Available online at www.sciencedirect.com

ScienceDirect

Underground Space 26 (2026) 197–219

www.keaipublishing.com/undsp

Research Paper

Influence of roughness on the mechanical response of rock-like specimens with nonpersistent joints under uniaxial compression based on joint deformation analysis

Hong Yin [a,b], Zehui Gao [a], Yulong Shao [b], Shuhong Wang [a,*], Jae-Joon Song [b], Ye Wang [a], Jineon Kim [b], Shan Guo [c]

[a] School of Resources and Civil Engineering, Northeastern University, Shenyang 110819, China
[b] Department of Energy Resources Engineering, Research Institute of Energy and Resources, Seoul National University, Seoul 08826, Republic of Korea
[c] State Key Laboratory for Tunnel Engineering, China University of Mining and Technology (Beijing), Beijing 100083, China

Received 8 May 2025; received in revised form 16 August 2025; accepted 20 September 2025
Available online 20 November 2025

Abstract

Joint deformation is a key factor controlling the mechanical behavior of discontinuous rock strata under changing stress conditions, including dominating the elastic deformation in near-surface excavations and serving as a major component of settlement under higher stress. This study, focusing on joint deformation behavior, investigates the effect of joint roughness on the peak stress and failure modes of specimens under uniaxial compression. Rock-like specimens with two layers of parallel, nonpersistent joints, one rough, were fabricated using 3D printing technology. Digital image correlation was used to capture real-time surface displacement fields, and a joint deformation analysis method was developed. The results show that joints exhibit staged, non-uniform closure and slip behavior, influenced by joint roughness, distribution of primary and secondary joints, and layered arrangement. Rough joints accelerate closure but hinder slip coordination, resulting in a three-stage loading process. In stage I, primary closure and layer-coordinated slip occur, accompanied by crack initiation, joint coalescence, and steady stress growth. Stage II involves secondary closure and overall coordinated slip, leading to localized failure and stress stabilization. Stage III is characterized by complete closure, uncoordinated slip, intensified crack propagation, and specimen failure, accompanied by stress hardening. The study reveals that joint deformation serves as a bridge linking roughness and peak strength. The average joint closure level and slip coordination are linearly negatively correlated with roughness but nonlinearly positively correlated with peak strength. Roughness restricts slip coordination, limiting crack propagation and delaying failure, which slows stress growth. Redistribution of joint aperture during slip reduces joint closure, weakens wall contact, and diminishes stress hardening.

Keywords: Jointed rock; Joint deformation; Crack propagation; Uniaxial compression

1 Introduction

Jointed rock mass failure under uniaxial compression is critical in tunnel excavation, slope stabilization, and mining. These failure modes directly impact engineering structure stability and safety (Cui et al., 2022; Zhang et al., 2023; Chen et al., 2015; Wang et al., 2023; Afolagboye et al., 2016). Rock mass mechanical properties are governed by joint geometric characteristics (Haeri et al., 2021), distribution patterns (Park & Bobet, 2009; Zhou et al., 2013; Huang et al., 2023), and deformation behavior (Li et al., 2024). Discontinuous joint behavior has attracted widespread attention (Pradhan & Siddique, 2020; Esterhuizen et al., 2011; Yang et al., 2020; Chen et al., 2012), particularly in underground pillar design (Brady & Brown, 2006), such as pillars (Fig. 1(a)) in underground mining

* Corresponding author.
E-mail address: shwang@mail.neu.edu.cn (S. Wang).
Peer review under the responsibility of Tongji University

https://doi.org/10.1016/j.undsp.2025.09.001

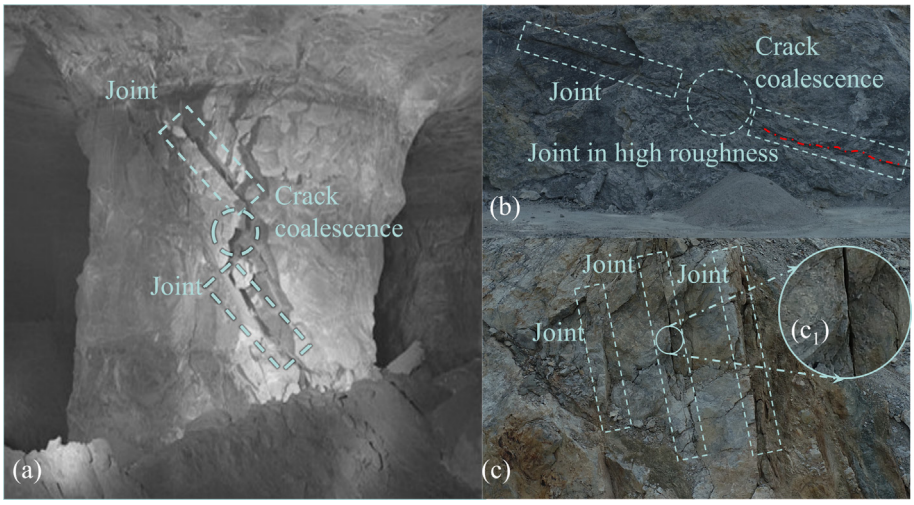

Fig. 1. Cases of failure in rock masses with rough nonpersistent joints under uniaxial compression. (a) Fracture along nonpersistent joints in underground pillars of a mine in the eastern and midwestern United States (Esterhuizen et al., 2011; Reproduced with permission, courtesy of Elsevier), (b) overall failure caused by rough nonpersistent joints in the cut rock slopes of an open-pit mine in Yingkou, Liaoning Province, China, (c) parallel layered joints in the cut rock slopes of an Al-Mg open-pit mine in Anshan, Liaoning Province, China, and (c_1) localized contact by joint slip.

operations (Esterhuizen et al., 2011), tunnel sidewalls (Fig. 1(b)), and cut slopes (Fig. 1(c)), which exhibit uniaxial compression stress states.

Research has focused on crack propagation and failure patterns using various detection methods, particularly acoustic emission monitoring (Alcott et al., 1998), and map microcrack distribution (Walton et al., 2017; Tang et al., 2019; Liu et al., 2019). Studies emphasize crack initiation criteria (Sih, 1974; Erdogan & Sih, 1963; Griffith, 1921; Jiao et al., 2024), evolution patterns (Lu et al., 2013; Huang et al., 2019), and macroscopic failure (Hoek & Bieniawski, 1965; Kumar et al., 2022). Joint closure behavior has been characterized (Bieniawski, 1967; Wang et al., 2019; Chen & Guo, 2020; Ye et al., 2021), but irreversible damage effects throughout loading receive limited attention (Xie et al., 2022; Li et al., 2024; Ren et al., 2022).

Joint closure directly influences joint wall contact behavior (Bandis et al., 1983), stress transmission, and crack propagation. The coupling between slip and closure behavior requires further investigation (Ren et al., 2023), particularly regarding joint length influence on deformation coordination, as illustrated in Fig. 1(c_1). Joint roughness significantly impacts rock mass behavior by altering wall contact conditions (Johansson & Stille, 2014), stress distribution (Asadizadeh et al., 2019), and crack propagation (Shan et al., 2025). Despite studies on rough joints (Wang et al., 2023; Hu et al., 2021), underlying mechanisms need exploration. Natural joints involve contact between rough surfaces (Cook, 1992), with rough joints resisting full closure and exhibiting inhibited slip. Therefore, explaining the influence of roughness on uniaxial compression performance from the perspective of joint deformation is an effective approach. Due to their significant undulations, rough joints are difficult to fully close, and their slip behavior is also notably inhibited. The mechanisms by which roughness affects joint closure and slip behavior, and how it influences the peak strength of rock masses through the control of crack propagation, require further investigation.

3D printing technology has enhanced experimental studies by precisely reproducing joint features (Gao et al., 2021; Ma et al., 2024). Compared to traditional specimen preparation methods, 3D printing technology enables the precise reproduction of joint geometric features, including roughness (Fereshtenejad & Song, 2021; Wang et al., 2023), spacing, and inclination (Shao et al., 2024b; Shao et al., 2024c), offering higher controllability and reproducibility for studies on joint closure and slip behavior. Specimens prepared using 3D printing technology can better simulate complex joint morphologies and their effects on the mechanical behavior of rock masses (Shao et al., 2024a; Cao et al., 2020; Wu et al., 2024).

This study employs 3D printing to fabricate controlled specimens containing two parallel discontinuous joints, one of which is rough, and uses digital image correlation (DIC) to capture full-field displacement during loading. By quantitatively characterizing joint closure and relative slip, the work elucidates how roughness governs crack propagation and peak strength. Based on a reconstructed coupled system representative of natural rock with coexisting smooth and rough joints, deformation characteristics at different joint layers and locations are systematically compared along with their sensitivity to roughness. The experimental results enable early risk-zone identification and localized support based on the spatial distribution of joint deformation, and allow inference of stress state and evolutionary stage from closure and slip signatures. The findings inform support design parameters, monitoring and warning thresholds, and construction sequencing strategies, thereby improving the accuracy of stability prediction and reducing support redundancy and operational risk.

2 Methodology

Figure 2(a) and (b) illustrates the geometric details of the test specimens, with dimensions of 100 mm × 100 mm × 30 m m (length × width × thickness). To achieve a comparative study of rough and smooth joints within a single specimen and better reproduce the multi-joint mechanical behavior of natural rock masses, two layers of parallel joints were set along the main diagonal direction of the specimen. To fully consider the positional effects of joints and the deformation characteristics of various parts within the joint body, each layer consists of nonpersistent double joints symmetrically distributed about the geometric center of the specimen, ensuring that each layer of joints is subjected to the same stress state. Starting from the top left and proceeding clockwise, the joints are named JA, JB, JC, and JD. The nominal length of the prefabricated joints is 50 mm, with an aperture of 1 mm, penetrating through the specimen along the thickness direction. Among these, JB and JC are smooth, while JA and JD are rough and are equally extracted from the same Barton's standard profile (Fig. 2(c)). To account for varying degrees of roughness, profiles No. 1, 4, 7, and 10 were selected at equal intervals. Each profile was divided into two parts at the center, digitized (Li & Zhang, 2015), and assigned to JA and JD of the same specimen, thereby constructing the 3D model of the specimen (Fig. 2(d)). The specimens are named TRQ-S, where T represents "test", R represents "roughness", Q indicates the number of smooth joints (0 or 2), and S represents the relative numbering of the rough profiles (1–4). Considering the stability of 3D printed specimens, one specimen was fabricated for each category (Fig. 3(a)).

The roughness coefficients of the digitized joints were calculated using the Z_2 and its relationship with the joint roughness coefficient (JRC) (Tse & Cruden, 1979) (Eq. (1)). The results are summarized in Table 1. It should be noted that for the two parts derived from profile No. 10, the JRC values calculated using Eq. (1) exceeded 20, which is beyond the range of Barton's standard profiles. Without loss of generality, these values were defined as 20 (Wang et al., 2023a).

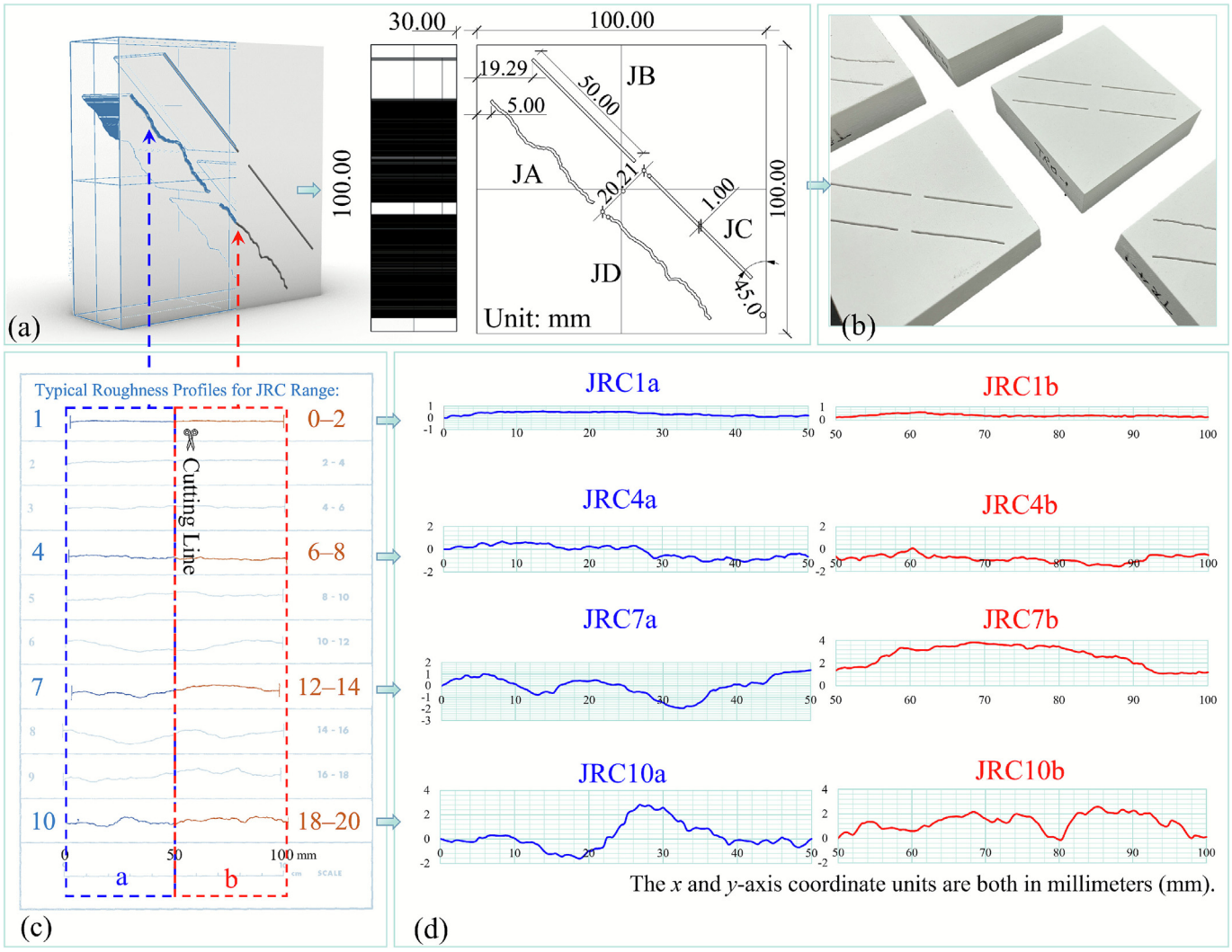

Fig. 2. Sample design. (a) Design diagram, (b) finished specimens, (c) typical profiles (Barton & Choubey, 1977), and (d) digitized profiles (Li & Zhang, 2015).

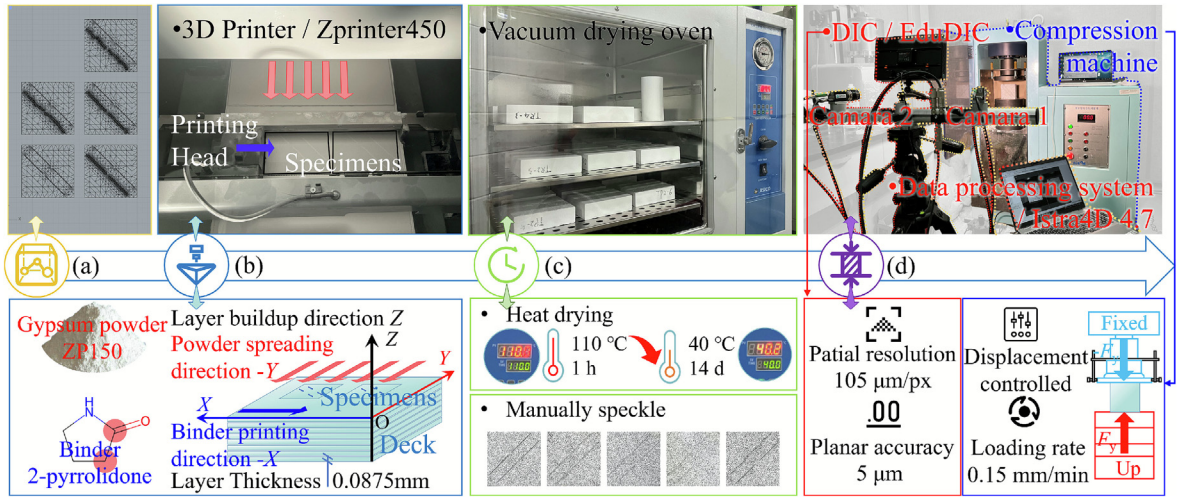

Fig. 3. Experiment workflow. (a) Modeling, (b) printing, (c) post-processing, and (d) testing.

Table 1
JRC of each joint after quantification.

Specimens	Roughness			No.
	JA	JD	JA/JD	
TR0-1	–	–	–	–
TR2-1	0.59	0.24	0.4	1
TR2-2	6.5	7	7.7	4
TR2-3	14.61	10.07	12.8	7
TR2-4	20	20	18.7	10

$$\begin{cases} \mathrm{JRC} = 32.2 + 32.47 \lg (Z_2) \\ Z_2 = \sqrt{\frac{1}{m(\Delta x)^2} \sum_{i=1}^{m} (y_{i+1} - y_i)} \end{cases}, \quad (1)$$

where JRC is the joint roughness coefficient, Z_2 is the root mean square of the slope, m is the number of sampling intervals, Δx is the sampling interval, and y_i is the height coordinate of ith sampling point.

Figure 3 illustrates the test procedure. 3D printing was adopted to precisely reproduce joint geometry and roughness, which is hard to achieve with natural rock. The 3D printer used was the Zprinter450, developed by 3D Systems. The printing material was gypsum powder (ZP150), which mainly consists of single-phase calcium sulfate hemihydrate ($CaSO_4{\cdot}0.5H_2O$) and partial anhydrous calcium sulfate ($CaSO_4$). During printing, the material undergoes a hydration reaction to generate stable calcium sulfate dihydrate ($CaSO_4{\cdot}2H_2O$) in the 3D printed specimens. The gypsum powder had a particle size range of 10–1000 μm and an average particle size of $d_{50} = 48.24$ μm. The binder used was 2-pyrrolidone, which provides excellent solubility and penetration properties for effective bonding between powder particles. The constructed digital model was printed along the direction perpendicular to the specimen thickness (Fig. 3(b)) with printing parameters of layer thickness 0.0875 mm and binder saturation 100%. After printing, the specimens were dried at 110 °C for 1 h and then maintained at 40 °C for 14 days (Fig. 3(c)). These two measures work together to effectively mitigate the influence of printing layers on the specimens (Yin et al., 2024; Shao et al., 2024a). Based on the above method, the physical and mechanical properties of natural weak sandstone can be simulated with high similarity. For details, please refer to the published work(Shao et al., 2024a; Shao et al., 2025). Following reinforcement treatment, uniaxial compression tests were conducted. The loading method was displacement-controlled, with a loading rate of 0.15 mm/min (Fig. 3(d)).

During the tests, the DIC technique was used to capture the surface displacement of the specimens in real-time (Fig. 3(d)). The DIC equipment was manufactured by Dantec Dynamics, model EduDIC, with a planar accuracy of 5 μm and a spatial resolution of 105 μm/px. The accompanying data processing system was Istra4D 4.7.

Figure 4(a) illustrates the principles of surface 3D digital correlation technology based on binocular imaging(Luo et al., 1993). By comparing images before and after deformation, corresponding points are matched using correlation functions to calculate displacement. The calculation accuracy depends on two key factors.

(1) Matching of left and right image points (Fig. 4(b)), which uses epipolar geometric constraints to construct a fundamental matrix $\boldsymbol{F}$, reducing the matching search from a 2D plane to a 1D epipolar line, thereby improving matching accuracy and robustness (Fig. 4(c)).
(2) Matching of image regions before and after deformation, which uses the sum of squared differences (SSD, C_{SSD}) function, Eq. (2), to achieve matching by minimizing grayscale value differences (Fig. 4(d)).

$$C_{\mathrm{SSD}} = \sum [G_t(x_t, y_t) - G(x, y)]^2, \quad (2)$$

where $G(x, y)$ represents the grayscale value of the reference region, which transforms into $G_t(x_t, y_t)$, after loading and deformation. By adjusting the illumination parameters

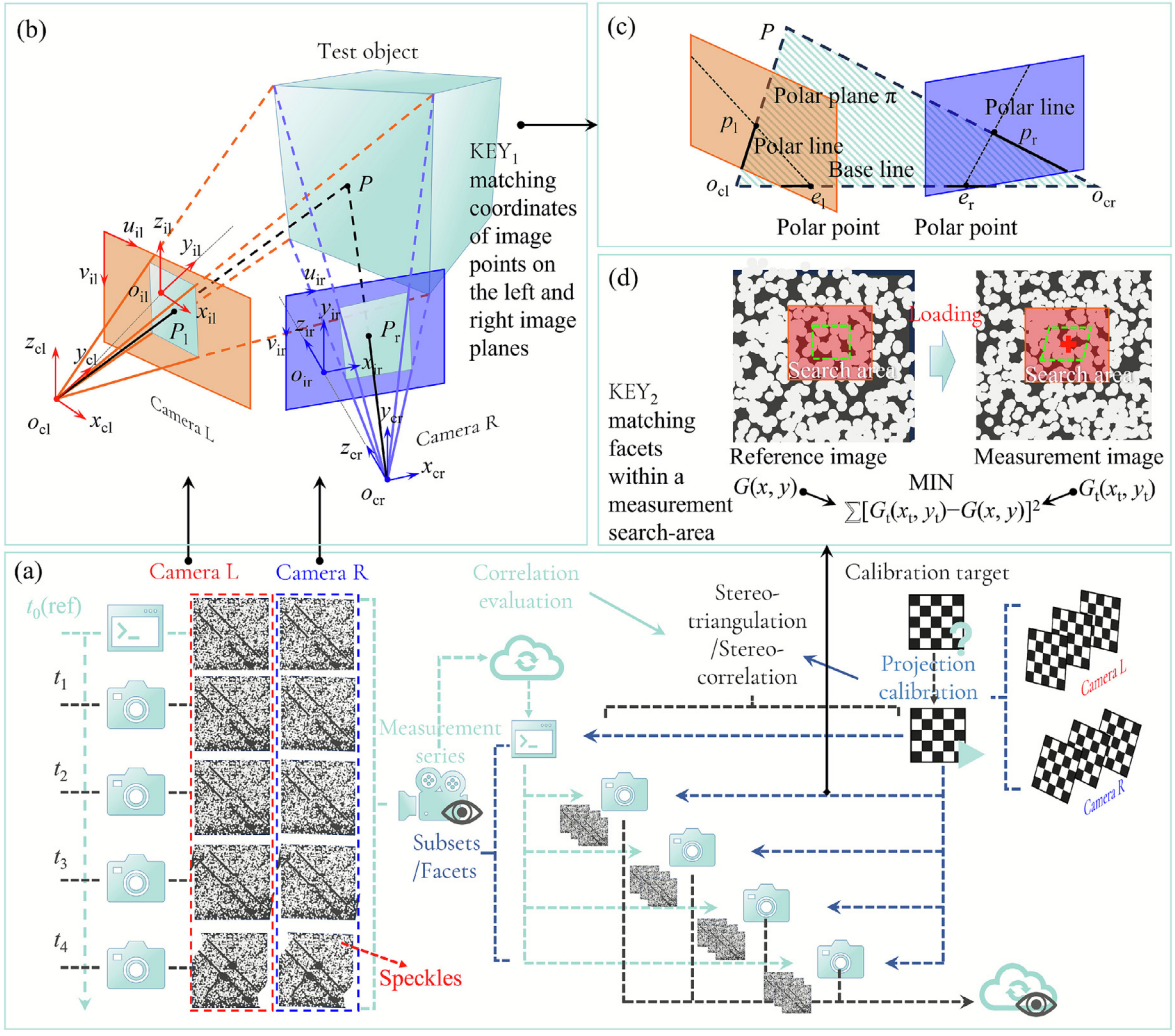

Fig. 4. Schematic diagram of the 3D DIC testing principle. (a) DIC measurement process, (b) stereo-triangulation, (c) principle of polar lines in geometry, and (d) facet matching.

and affine parameters during the calibration process, a matching accuracy of up to 0.01 pixels can be achieved.

Based on the above algorithm, the local deformation field is calculated sequentially. Using function fitting, the strain field is then obtained. The system provides multiple methods for strain field calculation, and in this study, the Lagrange strain is adopted (Eq. (3)).

$$\begin{cases} \varepsilon_{xx} = \frac{\partial u_p}{\partial x_p} + \frac{1}{2}\left[\left(\frac{\partial u_p}{\partial x_p}\right)^2 + \left(\frac{\partial v_p}{\partial x_p}\right)^2 + \left(\frac{\partial w_p}{\partial x_p}\right)^2\right] \\ \varepsilon_{yy} = \frac{\partial v_p}{\partial y_p} + \frac{1}{2}\left[\left(\frac{\partial u_p}{\partial y_p}\right)^2 + \left(\frac{\partial v_p}{\partial y_p}\right)^2 + \left(\frac{\partial w_p}{\partial y_p}\right)^2\right] \\ \varepsilon_{zz} = \frac{\partial w_p}{\partial z_p} + \frac{1}{2}\left[\left(\frac{\partial u_p}{\partial z_p}\right)^2 + \left(\frac{\partial v_p}{\partial z_p}\right)^2 + \left(\frac{\partial w_p}{\partial z_p}\right)^2\right] \\ \varepsilon_{xy} = \frac{1}{2}\left[\frac{\partial u_p}{\partial y_p} + \frac{\partial v_p}{\partial x_p}\right] + \frac{1}{2}\left[\frac{\partial u_p}{\partial x_p}\frac{\partial u_p}{\partial y_p} + \frac{\partial v_p}{\partial x_p}\frac{\partial v_p}{\partial y_p} + \frac{\partial w_p}{\partial x_p}\frac{\partial w_p}{\partial y_p}\right] \\ \varepsilon_{yz} = \frac{1}{2}\left[\frac{\partial v_p}{\partial z_p} + \frac{\partial w_p}{\partial y_p}\right] + \frac{1}{2}\left[\frac{\partial u_p}{\partial y_p}\frac{\partial u_p}{\partial z_p} + \frac{\partial v_p}{\partial y_p}\frac{\partial v_p}{\partial z_p} + \frac{\partial w_p}{\partial y_p}\frac{\partial w_p}{\partial z_p}\right] \\ \varepsilon_{xz} = \frac{1}{2}\left[\frac{\partial w_p}{\partial x_p} + \frac{\partial u_p}{\partial z_p}\right] + \frac{1}{2}\left[\frac{\partial u_p}{\partial x_p}\frac{\partial u_p}{\partial z_p} + \frac{\partial v_p}{\partial x_p}\frac{\partial v_p}{\partial z_p} + \frac{\partial w_p}{\partial x_p}\frac{\partial w_p}{\partial z_p}\right] \end{cases} . \quad (3)$$

In the equation, x_p, y_p, and z_p denote the coordinates of point P in the reference configuration. ε_{xx}, ε_{yy}, and ε_{zz} denote the normal components of the Lagrangian strain along the x , y, and z directions, respectively, representing extensional or compressional deformation; ε_{xy}, ε_{yz}, and ε_{zx} are the shear components of the Lagrangian strain corresponding to the xy, yz, and zx planes; u_p, v_p, and w_p are the displacement components of the point in the x, y, and z directions, respectively.

3 Results and discussion

3.1 Stress–strain curve

Figure 5(a)–(e) shows the stress–strain curves of the specimens under uniaxial compression. Unlike the typical stress–strain curves of brittle rocks (Eberhardt et al., 1999), the curves in this study are similar to the Type IV curves reported by Chen et al. (2013), exhibiting an overall stepwise trend before peak stress. This type is characteristic

of multi-jointed rock masses with a high joint connectivity ratio, as shown in Fig. 5(f). From the perspective of stress growth, the curves can be divided into four stages: stress climbing, stress stabilization, stress strengthening, and stress softening, with points *a*, *b*, and *c* marking the turning points between these stages. Point *c* corresponds to the peak stress of the specimen. Compared to the smooth curves in other stages, the stress climbing stage exhibits significant stress fluctuations, with the peaks and troughs of the fluctuations marked as points a_1, a_2, a_3, and a_4. In the stress stabilization stage, TR0-1 and TR2-1 show a slight trend of stress weakening, while TR2-2 demonstrates a slight stress strengthening trend. TR2-3 and TR2-4 exhibit a more pronounced stress strengthening trend. In the stress climbing stage, TR0-1 and TR2-1 display significant stress fluctuations, whereas the stress fluctuations in TR2-2, TR2-3, and TR2-4 are less prominent. Based on these characteristics, the stress–strain curves can be classified into two types: Type A includes TR0-1 and TR2-1, while Type B includes the rest (Fig. 5(f)). This classification cor-

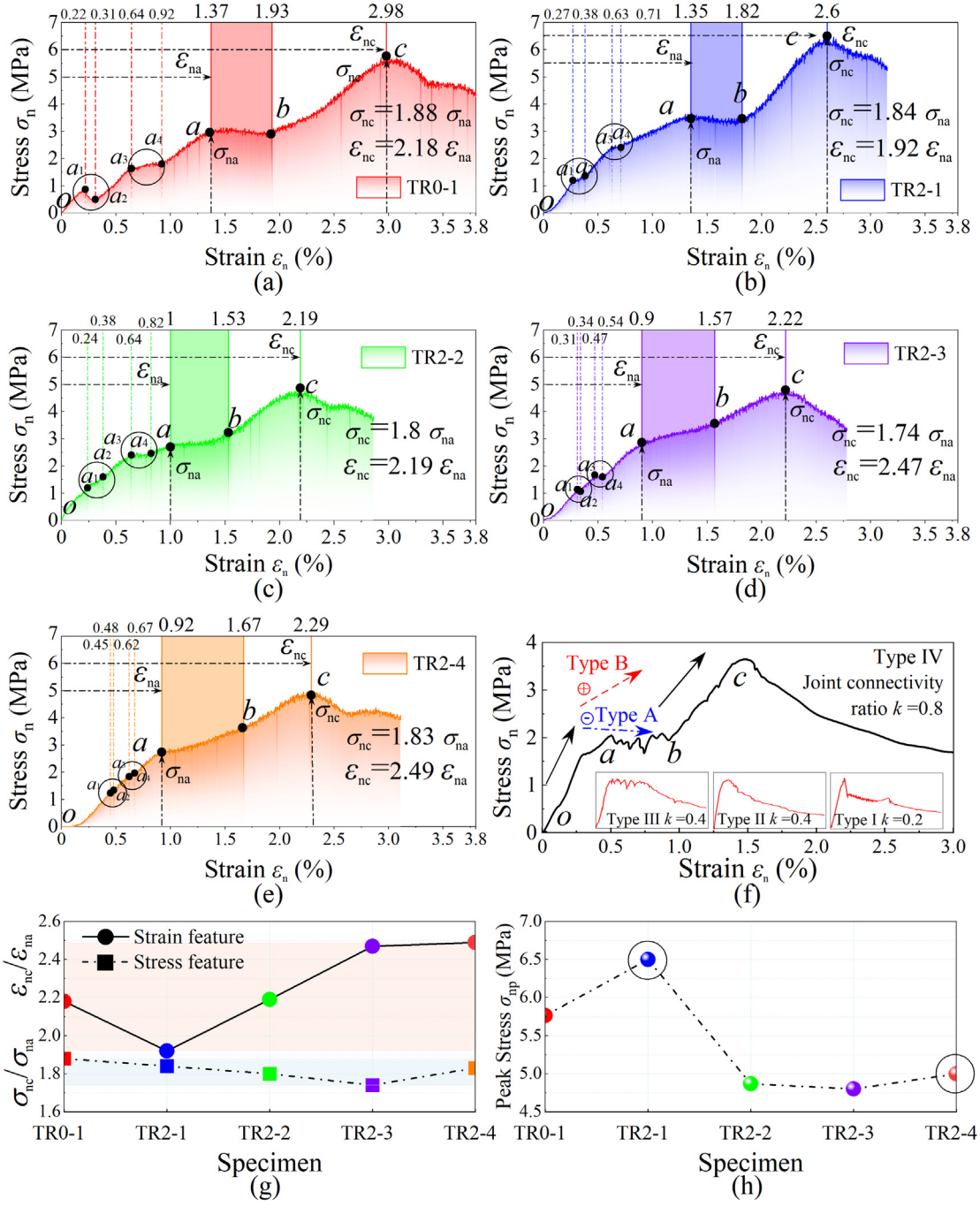

Fig. 5. Stress–strain curve characteristics. Stress–strain curve of specimen (a) R0-1, (b) R2-1, (c) R2-2, (d) R2-3, and (e) R2-4; (f) curve types, modified from Chen et al. (2013), (g) stress growth characteristics, and (h) peak stress variation.

responds to the trend of peak uniaxial compressive strength clustering shown in Fig. 5(h).

To further quantitatively analyze the contribution of each stage to the specimen's strength, the ratio of the strength at point c to the strength at point a (σ_{nc}/σ_{na}) was calculated for each specimen and summarized in the cyan region of Fig. 5(g). This ratio fluctuates between 1.73 and 1.88, centering around 1.8. These variations indicate that the stress climbing stage contributes more to the specimen's uniaxial compressive strength than the combined contributions of the stress stabilization and stress strengthening stages. For Type A curves, this combined contribution mainly comes from the stress strengthening stage. The stress σ_{na} at point a for each specimen approaches 3 MPa, so the difference in peak stress σ_{nc} between the specimens is attributed to the contributions of the stress stabilization stage and the stress hardening stage. Considering the linear relationship between strain and loading time, strain reflects the growth efficiency of the specimen's uniaxial compressive strength. The ratio of strain at point c to strain at point a ($\varepsilon_{nc}/\varepsilon_{na}$) was calculated for each specimen and summarized in the orange region of Fig. 5(g). This ratio fluctuates between 1.92 and 2.49, centering around 2.2. Combined with the characteristics of stress increment, the staged growth of stress and strain suggests that strength growth efficiency during the stress climbing stage is higher than that during the stress stabilization and stress strengthening stages.

In fact, the clustering trend of peak stress in Fig. 5(h) qualitatively indicates the weakening effect of rough joints on the uniaxial compressive strength of the specimens, which is consistent with the findings of Wang et al. (2025). However, some researchers have reported the opposite results. Yuan et al. (2023) observed a positive correlation between the uniaxial compressive peak strength of specimens containing persistent rough joints and joint roughness. B. Wang et al. (2023) and Asadizadeh et al. (2023) constructed numerical models of rock masses containing double rough discontinuous joints, showing a strengthening trend in peak compressive strength with increasing joint roughness. The mechanism by which rough joints weaken the uniaxial compressive strength of the specimens will be analyzed in subsequent sections.

3.2 Joint deformation

3.2.1 Joint deformation analysis based on displacement field and its mathematical expression

Due to the aperture of the pre-existing joint, specimen deformation during uniaxial compression is primarily concentrated on the pre-existing joint. The closure behavior of pre-existing joints significantly impacts specimen mechanical properties (Ren et al., 2023; Li et al., 2024), and this study also observes relative slip behavior along the joint axis. Figure 6 defines a method for calculating joint deformation based on DIC data. Point displacement in the XOY plane can be decomposed in two ways: (1) based on the coordinate system (red arrows in Fig. 6(a)), separating into X and Y direction displacements ($\boldsymbol{D}_X$, $\boldsymbol{D}_Y$), facilitating vector description using scalar components; (2) based on deformation direction (blue arrows in Fig. 6(a)) deformation into closure displacement ($\boldsymbol{D}_C$) perpendicular to the joint axis and slip displacement ($\boldsymbol{D}_S$) parallel to the joint axis.

By combining these methods, total displacement can be described through coordinate system decomposition, then further decomposed according to deformation direction (Fig. 6(b)). Since $\boldsymbol{D}_Y$ remains vertically upward in this study, joint movement analysis can be converted to analyzing $\boldsymbol{D}_X$ magnitude, which suits the DIC displacement field data (Fig. 3(b)).

To analyze joint deformation during loading, the relative displacement of observation points on both sides of the joint must be examined. While this is essentially a vector operation, the consistent vertical upward $\boldsymbol{D}_Y$ creates four basic combinations of relative displacement between points across the joint (Fig. 6(c)). Following the calculation method in Fig. 6(b), any $\boldsymbol{D}_C$ can be expressed as the vector sum of closure displacements ($\boldsymbol{D}_{CX}$, $\boldsymbol{D}_{CY}$) decomposed from X and Y directions. $\boldsymbol{D}_S$ can be expressed as the vector sum of slip displacements ($\boldsymbol{D}_{SX}$, $\boldsymbol{D}_{SY}$) decomposed from X and Y directions. The joint's relative displacement can be calculated using the following equation:

$$\begin{cases} \boldsymbol{D}_C = \boldsymbol{D}_C^U - \boldsymbol{D}_C^D = (\boldsymbol{D}_{CX}^U + \boldsymbol{D}_{CY}^U) - (\boldsymbol{D}_{CX}^D + \boldsymbol{D}_{CY}^D) \\ \boldsymbol{D}_S = \boldsymbol{D}_S^U - \boldsymbol{D}_S^D = (\boldsymbol{D}_{SX}^U + \boldsymbol{D}_{SY}^U) - (\boldsymbol{D}_{SX}^D + \boldsymbol{D}_{SY}^D) \\ \boldsymbol{D}_{CX} = \boldsymbol{D}_X / \cos\theta, \boldsymbol{D}_{CY} = \boldsymbol{D}_Y / \sin\theta \\ \boldsymbol{D}_{SX} = \boldsymbol{D}_X / \sin\theta, \boldsymbol{D}_{SY} = \boldsymbol{D}_Y / \cos\theta \end{cases}. \tag{4}$$

In Eq. (4), superscripts U and D denote the displacements of the measurement points located on the upper and lower sides of the joint. θ represents the angle between the direction of the $\boldsymbol{D}_C$ and the Y-axis, which is essentially determined by the angle between the joint axis and the horizontal direction. In this study, the reference value of θ is set to $\pi/4$. For rough joints, θ is a variable that changes with the position of the measurement point. However, considering the influence of the joint aperture and the overall effect of shear along the inclined plane, θ in some relatively smooth and gentle segments should also be taken as the angle between the joint axis and the horizontal direction. Special cases occur in certain segments of rough joints, as shown in Fig. 6(d). For joints with high roughness, vertical and horizontal segments may appear. In these cases, θ should be set to 0 and $\pi/2$, respectively, and the deformation displacement of the joint coincides with the displacement components decomposed based on the coordinate system. Equation (4) is then simplified to

$$\begin{cases} \boldsymbol{D}_C = \boldsymbol{D}_Y^U - \boldsymbol{D}_Y^D \\ \boldsymbol{D}_S = \boldsymbol{D}_X^U - \boldsymbol{D}_X^D \end{cases}, \tag{5}$$

$$\begin{cases} \boldsymbol{D}_C = \boldsymbol{D}_X^R - \boldsymbol{D}_X^L \\ \boldsymbol{D}_S = \boldsymbol{D}_Y^R - \boldsymbol{D}_Y^L \end{cases}. \tag{6}$$

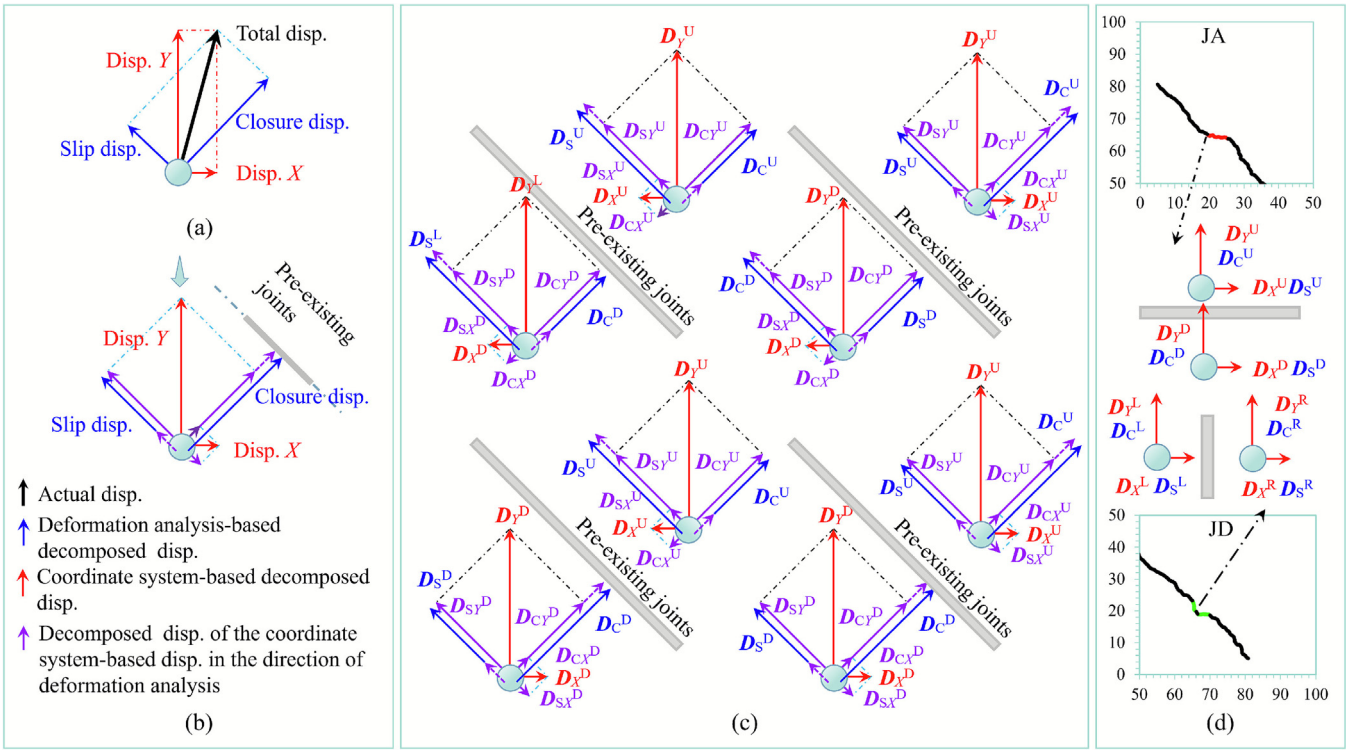

Fig. 6. Principles of joint closure and slip behavior analysis. (a) Two forms of displacement decomposition, (b) closure and slip displacement based on displacement from coordinate decomposition, (c) illustration of joint closure and slip behavior calculation, and (d) deformation behavior for special sections.

Four basic types in Fig. 6(c) show the influence of $\boldsymbol{D}_X$ on joint deformation. The relative magnitudes of $\boldsymbol{D}_X$ and $\boldsymbol{D}_Y$ are also critical factors. To address this, quadrants are introduced to transform vector operations into scalar operations.

As shown in Fig. 7(a), the displacement angle plane is formed with α_u (upper measurement point) as the horizontal axis and α_d (lower measurement point) as the vertical axis. Displacement angle is defined with horizontal leftward displacement as 0°, rotating clockwise to 180° when pointing horizontally right (Fig. 7(b)). Since $\boldsymbol{D}_Y$ remains vertically upward, both axes have a domain $[0, \pi]$.

With point $(\pi/2, \pi/2)$ as center and lines $u = \pi/2$, $d = \pi/2$ as boundaries, the plane divides into four displacement quadrants (I, II, III, IV). Joint deformation trend can be determined by comparing deformation displacements at corresponding points on both sides without calculating specific relative displacement values. Since the pre-existing joint angle θ with horizontal is $\pi/4$, trigonometric functions in Eq. (4) can be ignored. Table 2 shows the deformation trend determination equations for each quadrant.

In these equations, sgn is the sign function. x_1 and y_1 are $\boldsymbol{D}_X$ and $\boldsymbol{D}_Y$ components of the observation point above the joint (positive upward/rightward). x and y are displacement components below the joint (positive upward/rightward). For closure behavior: sgn $= -1$ indicates closure, sgn $= 0$ indicates relative static behavior along closure direction, sgn $= 1$ indicates opening. For slip behavior: sgn $= 0$ indicates no slip, sgn $= \pm 1$ indicates slip in opposite directions.

Before calculating joint deformation displacements, the closure and slip directions of any measurement point can be qualitatively determined based on the decomposition method shown in Fig. 6(b). As illustrated in Fig. 7(c), the domain $[0, \pi]$ can be divided into four continuous subdomains using $\pi/4$ as the scale, with uniquely determined closure and slip directions in each subdomain.

Joint deformation trends depend on the relative closure and slip directions of corresponding measurement points on both sides of the joint. Each quadrant of the displacement angle plane can be divided into four subregions using $\pi/4$ as the scale, with uniquely determined relative deformation modes in each subregion (Fig. 7(d)). When measurement points on both sides move toward each other, the joint exhibits closure and slip; when they move away from each other, it shows opening and slip; when they move in the same direction, the deformation trend requires further analysis.

In summary, the relative closure behavior of the joint in each displacement quadrant follows the following rules:

(1) For Quadrant I

- In subregion I_4, the measurement points on both sides move toward each other along the closure direction, and the joint exhibits closure.

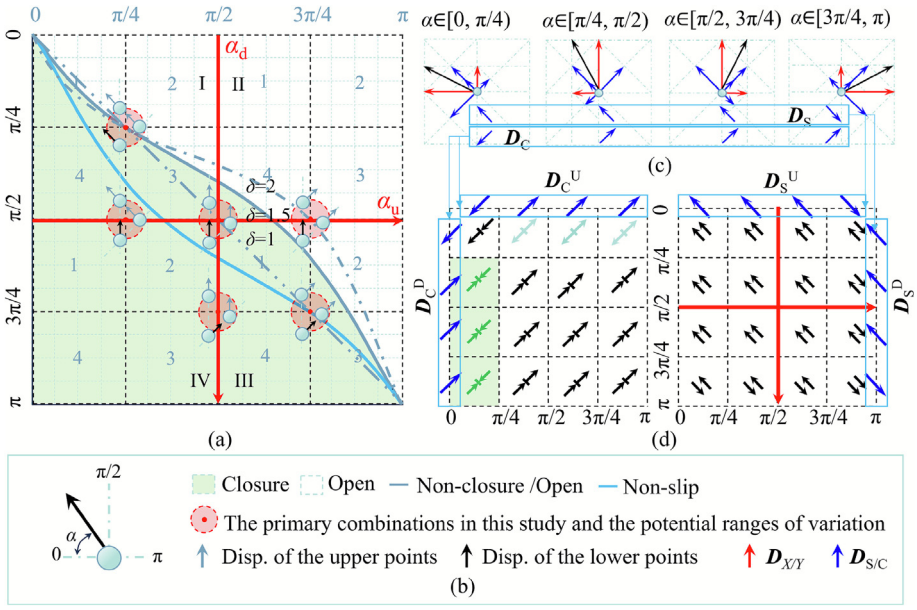

Fig. 7. Analysis principle of joint deformation. (a) Displacement-angle plane and partitioning of joint deformation trend, (b) definition of displacement angle and symbol notation, (c) displacement identification at individual point, and (d) bilateral point analysis for joint displacement mode.

Table 2
Determination criteria for deformation conditions in each displacement quadrant.

	I	II	III	IV
$\boldsymbol{D}_C$	$\mathrm{sgn}[(y_1 - x_1) - (y - x)]$	$\mathrm{sgn}[(y_1 + x_1) - (y - x)]$	$\mathrm{sgn}[(y_1 + x_1) - (y + x)]$	$\mathrm{sgn}[(y_1 - x_1) - (y + x)]$
$\boldsymbol{D}_S$	$\mathrm{sgn}[(y_1 + x_1) - (y + x)]$	$\mathrm{sgn}[(y_1 - x_1) - (x + y)]$	$\mathrm{sgn}[(y_1 - x_1) - (y - x)]$	$\mathrm{sgn}[(x_1 + y_1) - (y - x)]$

- In subregion I_2, the measurement points on both sides move away from each other along the closure direction, and the joint exhibits opening.
- In subregions I_1 and I_3, the measurement points on both sides move in the same direction along the closure direction. There exists a critical displacement angle at which the joint remains relatively static. Using the determination equation $\mathrm{sgn}[(y_1 - x_1) - (y - x)] = 0$, the critical displacement angle can be determined when $y_1 - x_1 = y - x$, $x_1 - y_1 = x - y$.

(2) For Quadrant II

- In subregion II_{12}, the measurement points on both sides move away from each other along the closure direction, and the joint exhibits opening.
- In subregion II_{34}, the measurement points on both sides move toward each other along the closure direction. There exists a critical displacement angle at which the joint remains relatively static. Using the determination equation $\mathrm{sgn}[(y_1 + x_1) - (y - x)] = 0$, the critical displacement angle can be determined when $y_1 + x_1 = y - x$.

(3) For Quadrant III, the two points move in the same direction along the closure direction

- In subregion III_4, considering the distribution pattern of the $\boldsymbol{D}_Y$ field along the main diagonal, which decreases from the lower region through the middle region to the upper region (Yin et al., 2024), it is always true that $y > y_1$. According to Figs. 7(c) and (d), $x > y$, $y_1 > x_1$ and thus $x > x_1$. Therefore, $y + x$ is always greater than $y_1 + x_1$, and the joint exhibits closure.
- For other subregions, the critical displacement angle can be determined using the determination equation $\mathrm{sgn}[(y_1 + x_1) - (y + x)] = 0$, which is satisfied when $y_1 + x_1 = y + x$.

(4) For Quadrant IV

- In subregion IV_{14}, the measurement points on both sides move toward each other along the closure direction, and the joint exhibits closure.
- In subregion IV_{23}, the two points move in the same direction along the closure direction. Since $y > y_1$, it follows that $y + x > y_1 - x_1$, and the joint exhibits closure.

The critical displacement angle that ensures the joint remains relatively stationary is determined below. Taking the third displacement quadrant as an example, the critical position is

$$y_1 + x_1 = y + x. \tag{7}$$

Dividing both sides by y_1, the equation becomes

$$1 + x_1/y_1 = y/y_1 + x/y_1. \tag{8}$$

By letting $x = y/\tan\alpha_d$, $x_1 = y_1/\tan\alpha_u$, and $y/y_1 = \delta$, substituting these into Eq. (8) gives:

$$1 + 1/\tan\alpha_u = \delta + \delta/\tan\alpha_d. \tag{9}$$

Solving for α_u yields:

$$\alpha_u = \pi - \tan^{-1}\left(\frac{1}{\delta(1/\tan(\pi-\alpha_d)+1)-1}\right), \alpha_d \in \left[\frac{\pi}{2},\pi\right] \alpha_u \in \left[\frac{\pi}{2},\pi\right]. \tag{10}$$

In a similar manner, the critical positions for the second and first displacement quadrants are determined as

$$\alpha_u = \pi - \tan^{-1}\left(\frac{1}{\delta(1-1/\tan(\pi-\alpha_d))-1}\right), \alpha_d \in \left[0,\frac{\pi}{2}\right] \alpha_u \in \left[\frac{\pi}{2},\pi\right], \tag{11}$$

$$\alpha_u = \tan^{-1}\left(\frac{1}{1-\delta(1-1/\tan(\pi-\alpha_d))}\right), \alpha_d \in \left[0,\frac{\pi}{2}\right] \alpha_u \in \left[0,\frac{\pi}{2}\right]. \tag{12}$$

The segmented curve defines the closed critical line in the coordinate system (Fig. 7(a)), with the region below representing joint closed state and the region on/above representing non-closed state. For joint slip, a non-slip state exists only at specific positions, shown by the non-slip curve. During loading, joint deformation is governed by the closed state, appearing as superimposed slip and closure/non-closure.

In Eq. (9), δ represents the ratio of $\boldsymbol{D}_Y$ below the joint to that above. Different δ values form curve families passing through the first displacement quadrant center ($\pi/4$, $\pi/4$). Higher δ values shift the curve intersections: with $\alpha_d = \pi/2$ rightward and with $\alpha_u = 3\pi/4$ upward. The closed region expansion in areas I_3, II_4, and III_{123} exceeds the reduction in I_1, indicating that joint closure is sensitive to δ.

Figure 6(a) helps analyze deformation trends in multi-joint structures. The red disk in Fig. 7(a) shows the conditions of this study, with its center representing the fundamental deformation mode and radius showing displacement angle variations. Joints predominantly exhibit closed state deformation with some opening behavior. As loading progresses, δ increases and opening behavior diminishes, explaining why joint opening typically occurs early in loading. The parameter δ reflects $\boldsymbol{D}_Y$ distribution patterns, influenced by the Poisson effect.

3.2.2 Displacement line distribution on the specimen surface and sample point selection

The displacement decomposition and deformation calculation methods from Section 3.2.1 can be used to quantitatively calculate joint closure and slip at different times, locations, and sections, which is crucial for analyzing jointed rock mass fracture processes. Sampling sections are determined at key joint locations by considering closure and slip conditions at the joint tip and along the joint body, with increased sampling density for rough joints. As shown in Fig. 8(a), sample points slightly deviate from the joint contour edge due to limitations in DIC technology.

Shape edge detection typically employs pixel-level algorithms that can only approximate edge locations due to precision constraints. As illustrated in Fig. 8(a_1), the actual sample point P' is separated from the designed sample point P by a distance d, which can be decomposed into a vertical component d_1 and a horizontal component d_2. Figure 8(b) shows six sample lines of different orientations and lengths, and Fig. 9(a)–(d) presents the standard deviations of displacements along these lines throughout the loading process. The curves indicate that displacement variation decreases as sample lines shorten, with Fig. 9(e) showing near-zero displacement standard deviations for the shortest lines. Since d_1 and d_2 are much smaller than the lengths of sample lines 4 and 5, the effect of sample point position deviation on final results can be considered negligible.

3.2.3 Deformation of the joint body

Figure 10 shows the variation curves of closure and slip displacements for different parts of the joint body with strain, conforming to the nonlinear characteristics revealed by Goodman (1974). According to the notation in Section 3.2.1, positive growth in closure displacement curves indicates joint opening, while negative growth indicates closure. At any moment, positive closure displacement represents opening relative to the initial state, while negative values indicate closure. For slip displacement curves, positive growth indicates clockwise slip, while negative growth indicates counterclockwise slip.

Based on the stress–strain curve stages defined in Fig. 5, the time-history diagram in Fig. 10 marks the deformation characteristics of the joint body at each stage. This study primarily focuses on joint deformation characteristics before peak stress.

(1) Common characteristics

(1.1) The closure displacement curves (Fig. 10(a_1)) for all joints exhibit a general trend of negative increase, with some joints showing localized positive increases in the $oa_{3/4}$ segment. The curve following $a_{3/4}$ exhibits a hyperbolic-like characteristic, as described by Goodman (1974). The slip displacement curves (Fig. 10(a_2)) for all joints show a trend of positive increase. This indicates that the joints in all specimens predominantly exhibit closure-slip behavior, consistent with the analysis in Section 3.2.1.

(1.2) Joint displacement curves are divided into two groups (Fig. 10(a)). For closure displacement: JA and JC (main joints) show similar closure behavior; JB and JD (subordinate joints) also exhibit closure but with opening behavior in the $a_{1/2}a_{3/4}$. During stress climbing (oa) and stabilization (ab) stages, JA/JC curves are generally lower than JB/JD curves. For slip displacement: JA and JD show similar trends, as do JB and JC, with JA/JD curves generally higher than JB/JC during oa and ab. These patterns indicate that closure behavior is significantly influenced by main/subordinate joint (Yin et al., 2024) distribution (main joints close faster), while slip displacement is more affected by joint layer distribution (layers closer to the primary loading direction slip faster).

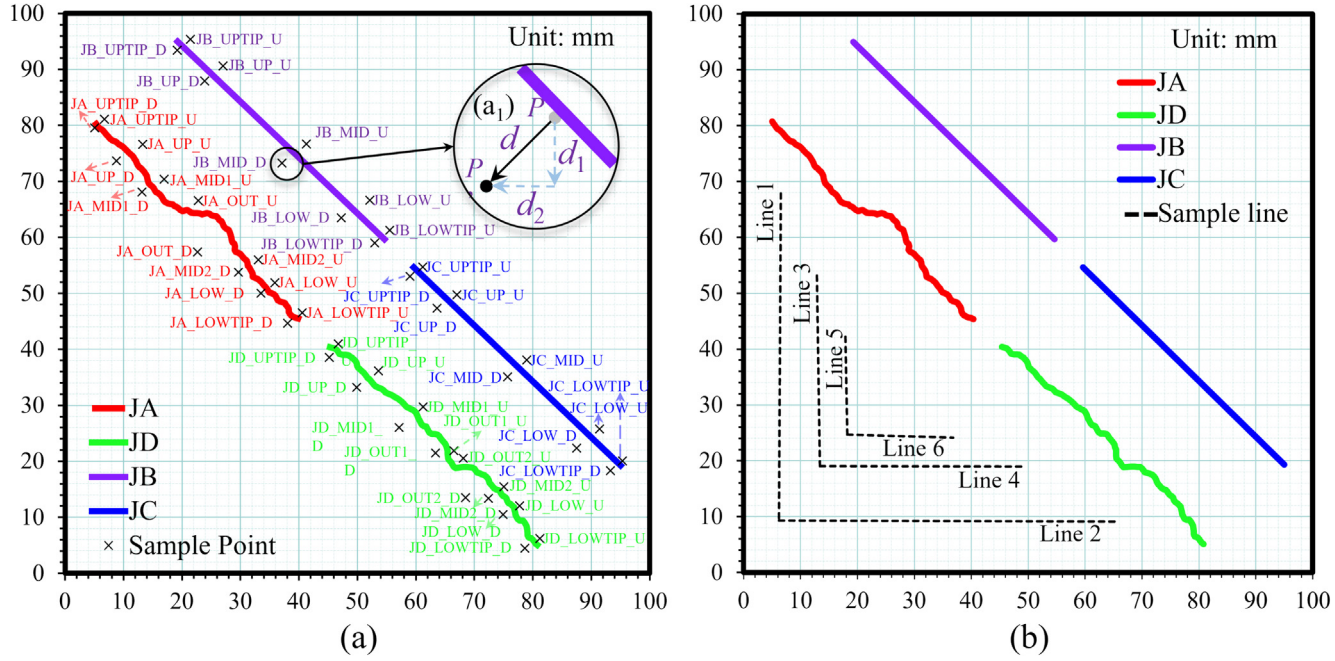

Fig. 8. Sampling location diagram. (a) Sample points for calculating joint deformation, and (b) sample lines for analyzing displacement distribution.

(1.3) Displacement curves of different parts within the same joint location show variability (Fig. 10(a)). Slip displacement curves are generally more concentrated than closure displacement curves. For closure displacement: JA and JC curves start closely distributed and gradually disperse before eventually converging; JB and JD curves begin dispersed and gradually converge, with JC curves eventually intersecting. For slip displacement: all joint curves transition from concentrated to dispersed distributions, with JB and JC showing greater dispersion than JA and JD. These patterns indicate non-uniform closure-slip behavior along the joint axis during loading.

(1.4) The closure displacement curves of different parts of the same joint location can be divided into two groups based on their shapes and proximity (Fig. 10(b)). For JA and JB, the curves can be divided into UP curves and MID_LOW curves. For JC and JD, the curves can be divided into LOW curves and UP_MID curves. This indicates that the closure behavior of parts near the specimen edges is relatively independent. This will be further explained in subsequent discussions on the relationship between joint tip motion and the initiation of propagating cracks.

(1.5) The displacement curves of different parts of the same joint location exhibit consistent distribution patterns (Fig. 10(b)). For closure displacement: in JA and JD, the UP curves are positioned lowest (greatest negative increase), followed by MID curves, with LOW curves highest (least negative); JB and JC show the opposite pattern, with LOW curves lowest, followed by MID curves, and UP curves highest. For slip displacement: in JA and JD, the UP curves are positioned highest (greatest positive increase), followed by MID curves, with LOW curves lowest; JB and JC show the opposite pattern, with LOW curves highest, followed by MID curves, and UP curves lowest. These findings indicate that closure-slip behavior ordering across different joint parts is significantly influenced by joint layering: JA and JD exhibit progressive closure-slip behavior from top to bottom along their axis, while JB and JC exhibit progressive behavior from bottom to top.

(2) Unique characteristics

(2.1) In TR0-1, the closure displacement curves of all joints intersect in the *bc* stage, reaching the same closure displacement. At the stress peak, the curves remain relatively stationary or increase slowly. This indicates that the final level of joint closure is independent of its location.

(2.2) Regarding closure displacement (Fig. 10(a_1)): in all specimens, JB and JC reach a displacement difference threshold of 1 in the *bc* stage (indicating complete closure) and remain relatively stable at peak stress; in TR2-2, TR2-3, and TR2-4, JA and JD fail to reach the displacement difference threshold of 1. For slip displacement (Fig. 10(a_3)): in TR0-1, JA and JD exhibit greater slip speed and magnitude than JB/JD; in TR2-series specimens, the slip speed of JA and JD decreases during the *ab* and is eventually surpassed by JB and JC. This indicates that joint roughness impedes complete closure and slip. During slip, apertures between rough joint surfaces redistribute, as confirmed by Cook (1992). Areas with reduced aperture obstruct further closure, a phenomenon more pronounced in joints with greater roughness (Zhang et al., 2024; Hopkins, 2000). Specimens with persistent joints exhibit shear behavior under uniaxial compression, consistent with shear mechanics (Wang et al., 2021). In studies by B. Wang et al.(2023)

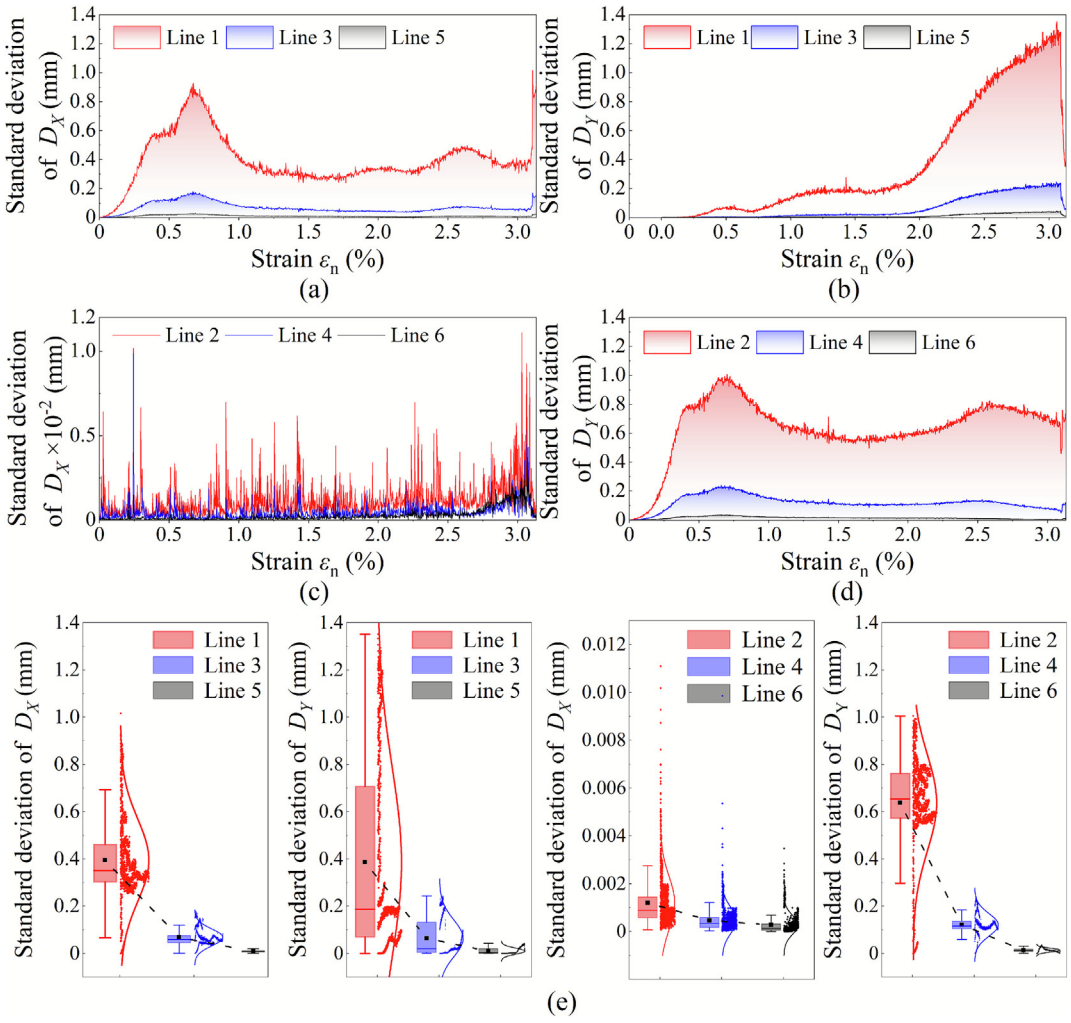

Fig. 9. Line distribution patterns of surface displacement. (a) Line distribution pattern of $\boldsymbol{D}_X$ along Y-axis, (b) line distribution pattern of $\boldsymbol{D}_Y$ along Y-axis, (c) line distribution pattern of $\boldsymbol{D}_X$ along X-axis, (d) line distribution pattern of $\boldsymbol{D}_Y$ along X-axis, and (e) consistency pattern in displacement line distribution.

and Asadizadeh et al. (2019), the joints in specimens had lower persistence, with a higher proportion of intact rock. Therefore, the strength was primarily contributed by crack propagation and specimen failure, while the low persistency rate restricted joint slip behavior and aperture redistribution. Once the joints became fully connected, they could close completely, and at this point, under overall slip action, the strengthening effect of roughness on peak strength manifested as shear behavior. In the study of Wang et al. (2025) and this research with high-persistence joints, peak strength was primarily determined by the degree of joint closure.

(2.3) Comparing the closure behavior of JA and JC across specimens (Fig. 10(b)). In TR0-1, JA and JC both close rapidly during the $a_{1/2}b$ and remain relatively stationary during the bc. In TR2-1 and TR2-2, JC closes rapidly during the $a_{1/2}a$ and remains stationary or continues closing during the ac, while JA closes rapidly during the $a_{1/2}a_{3/4}$ and remains stationary or continues closing during the $a_{3/4}c$. In TR2-3 and TR2-4, JC closes rapidly during the $a_{1/2}b$ and remains stationary or continues closing during the bc, while JA closes rapidly during the $a_{1/2}a$ segment and remains stationary or continues closing during the ac stage. Combined with (1.3), this indicates that roughness characteristics advance and accelerate joint closure behavior, shortening the time required to reach maximum closure capacity.

(2.4) The closure displacement curves of different parts of JB and JD in all specimens exhibit the same trend (Fig. 10(b)). For JD, the lower curve opens during the $a_{1/2}a_{3/4}$ and closes rapidly during the $a_{3/4}c$, while the middle-upper curve closes rapidly during the $a_{1/2}c$. For JB, the upper curve opens during the $a_{1/2}a_{3/4}$ and closes rapidly during the $a_{3/4}c$, while the middle-lower curve closes rapidly during the $a_{1/2}b$ and continues closing during the bc. Combined with (2.3) and (1.2), this indicates that joint closure speed is influenced by both the main or subordinate position and roughness, with the influence of the main or subordinate position being more significant.

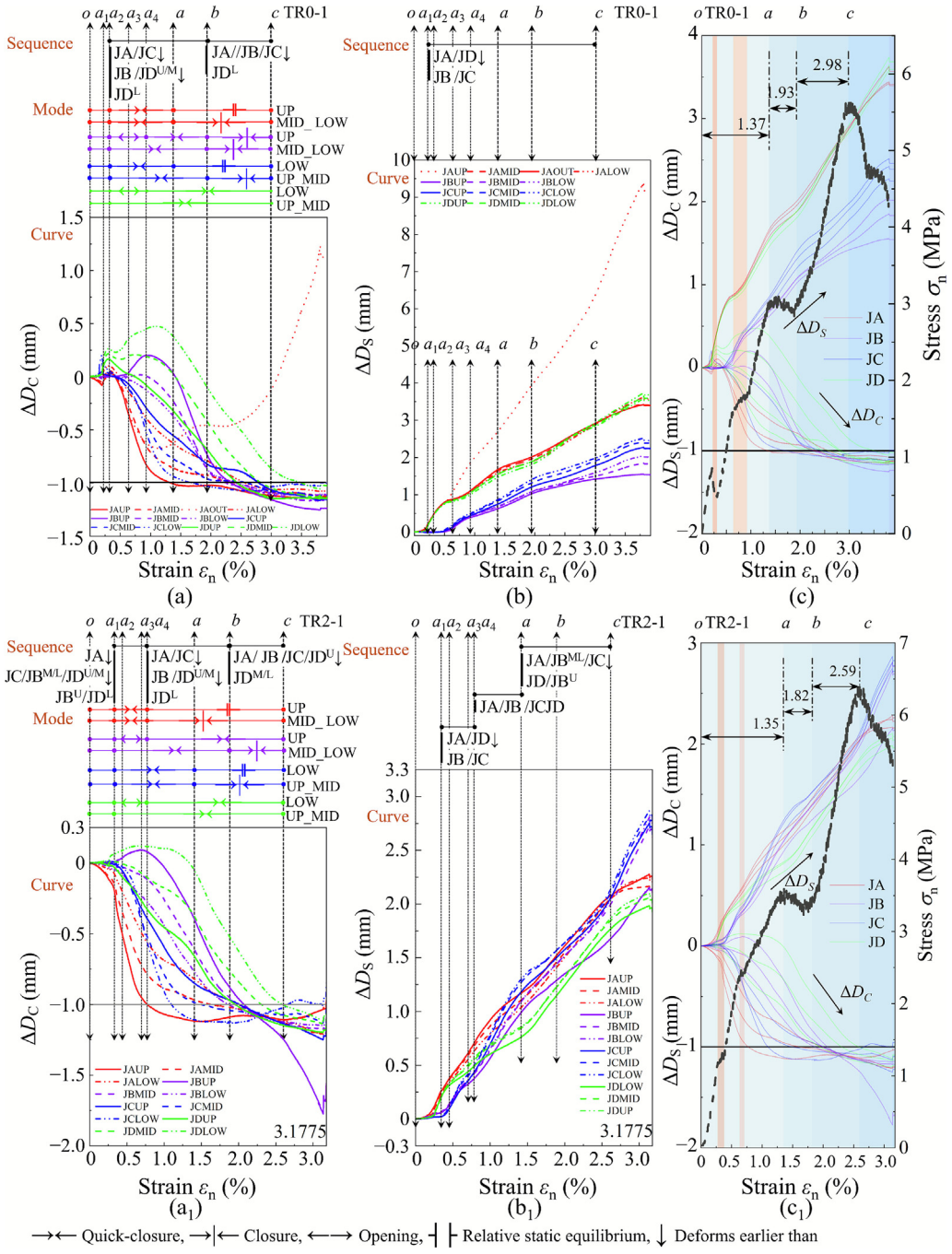

Fig. 10. Analysis of deformation of joint bodies. (a) Joint closure characteristics, (b) joint slip characteristics, and (c) correlation between joint deformation and stress–strain curves of specimen R0-1. (a_1) Joint closure characteristics, (b_1) joint slip characteristics, and (c_1) correlation between joint deformation and stress–strain curves of specimen R2-1. (a_2) Joint closure characteristics, (b_2) joint slip characteristics, and (c_2) correlation between joint deformation and stress–strain curves of specimen R2-2. (a_3) Joint closure characteristics, (b_3) joint slip characteristics, and (c_3) correlation between joint deformation and stress–strain curves of specimen R2-3. (a_4) Joint closure characteristics, (b_4) joint slip characteristics, and (c_4) correlation between joint deformation and stress–strain curves of specimen R2-4.

(2.5) For the special sampling points in Fig. 8, their corresponding deformation capacity is significantly enhanced, and the enhancement of slip and closure capacity is mutually exclusive. For example, in TR2-4, sampling point JD_OUT1 corresponds to a vertical joint segment, resulting in significantly enhanced slip capacity, but its closure displacement increases positively, indicating intense opening. Sampling point JD_OUT2 corresponds to a horizontal joint segment, resulting in significantly enhanced closure capacity, but its slip displacement curve flattens.

Based on observations, specimen displacement curves can be divided into stages according to joint closure level. Joint roughness advances and accelerates closure behavior, transforming closure displacement curves from a three-

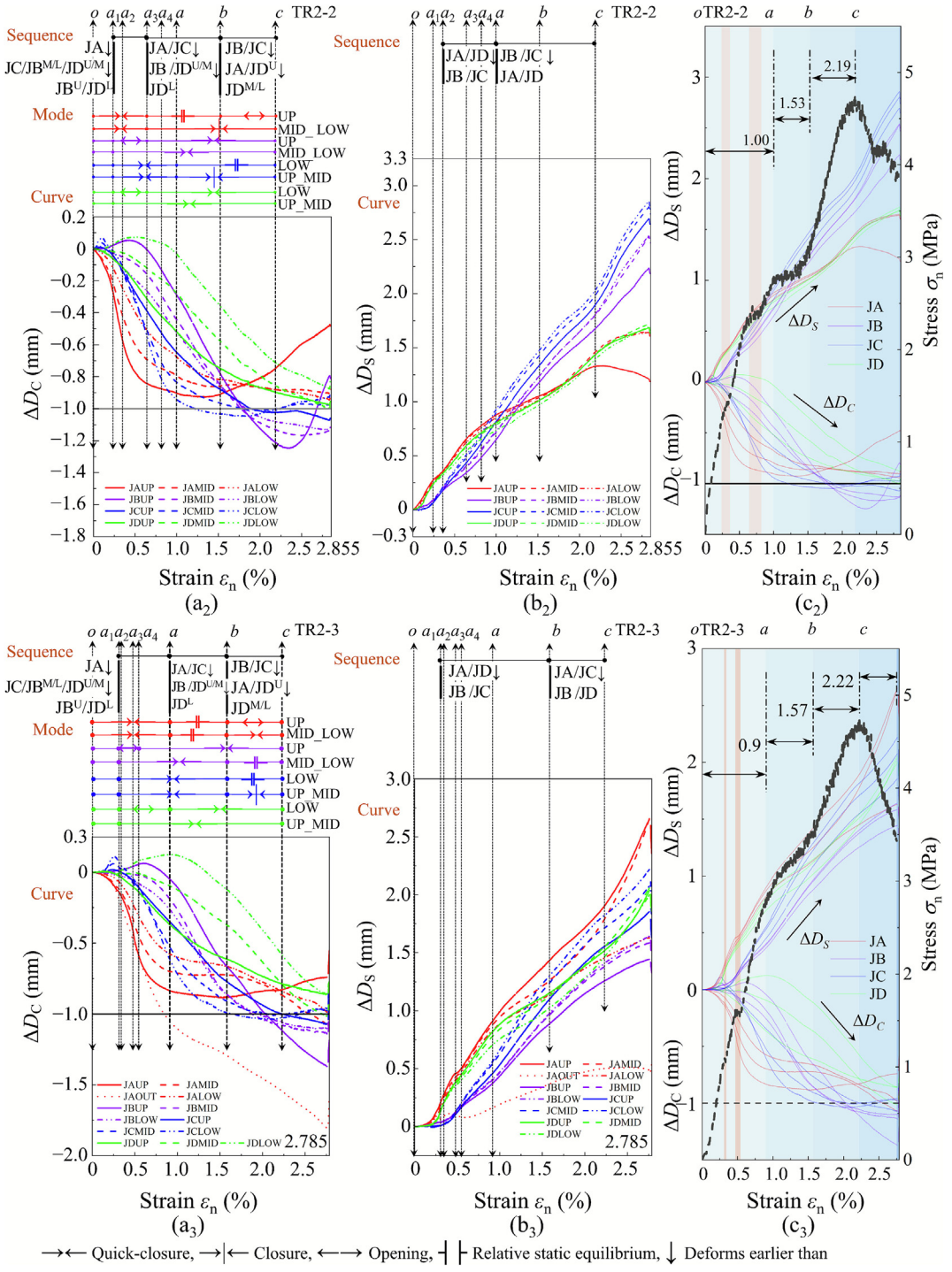

Fig 10. *(continued)*

stage pattern of TR0-1 to a four-stage pattern in other specimens. Similarly, roughness hinders slip capacity, changing slip displacement curves from a two-stage pattern of TR0-1 to a four-stage pattern in other specimens. The inflection points in joint deformation displacement curves correspond to stage boundaries in the stress–strain curves shown in Fig. 5. From the joint body deformation perspective, this can be described as Fig. 10(c).

- The *oa* (stress climbing stage) represents the primary closure and layer-coordinated slip stage of the joints. Within the $oa_{1/2}$, joint deformation displacement initiate; during the $a_{1/2}a_{2/4}$, the main joints close rapidly, subordinate joints open locally, and upper and lower layer joints slip in the layer with similar capacities; during the $a_{2/4}a$, the main joints close locally and completely, subordinate joints transition from local

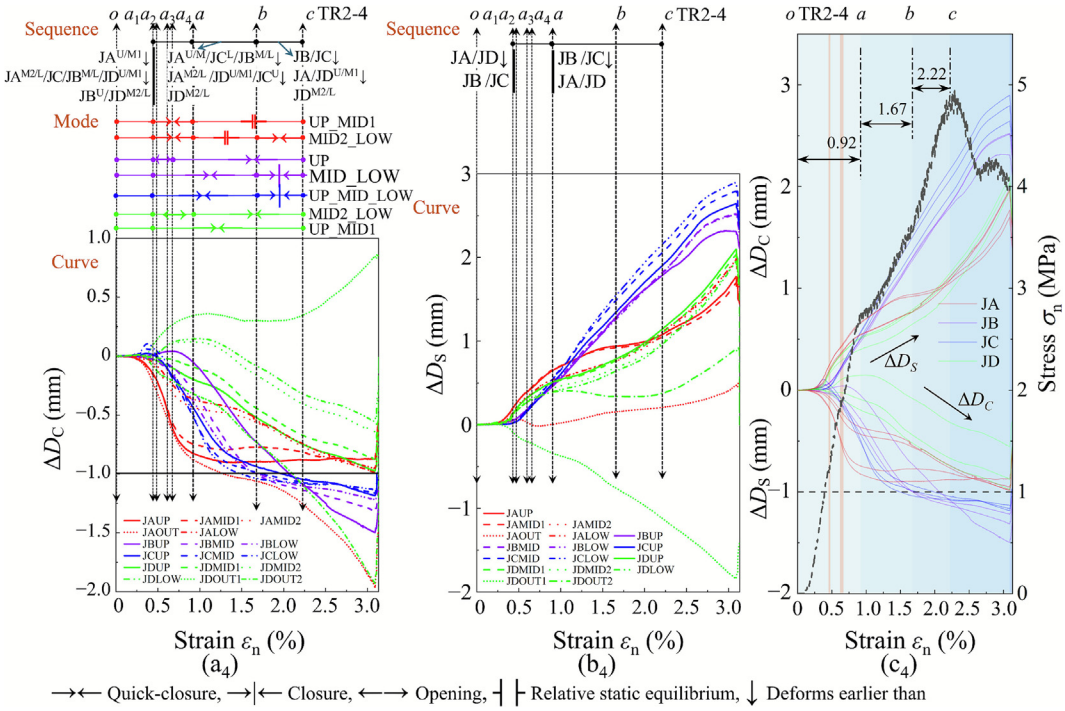

Fig 10. *(continued)*

opening to overall rapid closure, and upper and lower layer joints gradually converge to similar slip capacities.

- The *ab* (stress stabilization stage) represents the secondary closure and overall coordinated slip segment. During this stage, the main joints tend toward complete closure, subordinate joints close rapidly, and the slip capacities of upper and lower layer joints become similar.
- The *bc* (stress strengthening stage) represents the complete closure and overall uncoordinated slip segment of the joints. During this stage, the main and subordinate joints achieve maximum closure capacity overall, with local continued closure, and the slip capacities of different parts of the upper and lower layer joints exhibit significant dispersion.

The maximum principal strain cloud diagrams at stress–strain curve stage boundaries (Fig. 11) show that increasing joint roughness reduces crack propagation and failure extent at equivalent boundary points, indicating roughness hinders complete specimen failure and prevents full realization of compressive capacity.

This analysis explains failure phenomena in Fig. 11. The *oa* represents primary joint closure and layer-coordinated slip, characterized by rapid crack propagation, joint coalescence, and specimen fracturing that releases compressive capacity and forms the stress climbing stage. The *ab* involves secondary closure and overall coordinated slip, where main joints close completely, specimens experience local failure, and stress stabilizes within a certain range. The *bc* features complete closure and overall uncoordinated slip, with joint walls making contact to form stress strengthening until specimens completely fail.

3.2.4 Joint tip deformation and initiation of propagating cracks

The closure and slip displacements at the joint tips of each specimen were calculated in Fig. 12. Since the joint tips are only related to crack initiation, and considering the missing DIC data at certain time steps caused by instantaneous rupture, only the displacement curves during the stress climbing stage were analyzed. The specific time steps were determined based on the maximum time step at which DIC could simultaneously capture data for all eight tips of the four joints, and all selected time steps were greater than the time step corresponding to a_2.

Overall, the displacement curves of the specimens exhibit similar trends. The main characteristics of the closure displacement curves are as follows:

- The lower tips of JA and JB, along with the upper tips of JC and JD exhibit the same trend (highlighted in Fig. 12 (a)): after initial micro-closure fluctuation, they grow negatively, indicating closure. The lower tip of JC displays a unique pattern: after micro-closure fluctuation, its displacement curve first grows rapidly positive, then negative, showing initial opening followed by closure, a phenomenon rarely addressed in existing joint closure studies. The upper tip of JA demonstrates another distinct pattern: after micro-closure fluctuation, it first grows rapidly negative before transitioning to positive displacement, indicating initial closure followed by sud-

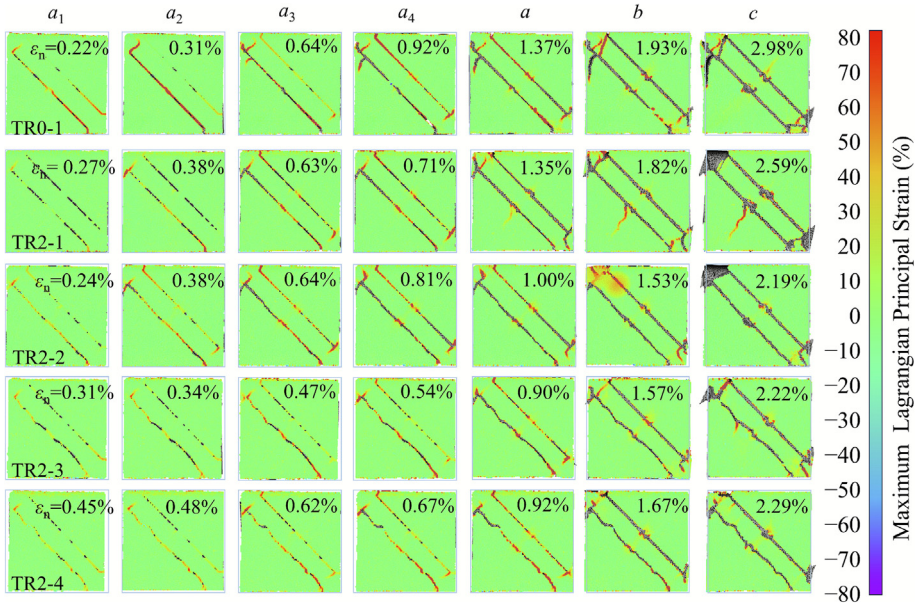

Fig. 11. Maximum principal strain contour map.

den opening. For the upper tip of JB and the lower tip of JC, after micro-closure fluctuation, the displacement curves gradually grow positive, indicating joint opening.

- The upper tip of JA and the lower tip of JD are the first to initiate closure displacement, while the lower tip of JA, the upper tip of JD, and both the upper and lower tips of JB and JC exhibit delayed and synchronized initiation of closure displacement.
- The closure displacement of all joint tips initiates before point a_1.

Compared to the closure displacement curves, the slip displacement curves of the specimens exhibit stronger consistency, with the main characteristics as follows:

- The displacement curves first experience a micro-slip fluctuation phase during the loading process, followed by a rapid positive increase in slip displacement. This indicates that the lower measurement point at the joint tip slides diagonally upward along the main diagonal, while the upper measurement point slides diagonally downward along the main diagonal.
- The displacement curves exhibit a significant grouping phenomenon, where the upper and lower tips of JA and JD form one group, and the upper and lower tips of JB and JC form another group. The slip displacement of the tips of JA and JD initiates earlier than that of JB and JC, and the slip displacement of the tips of JA and JD is greater than that of JB and JC. The difference between the two groups gradually decreases after the slip displacement of the tips of JB and JC is initiated.
- The slip displacement of the upper and lower tips of JA and JD initiates before point a_1.

The above characteristics indicate that the oa_1 can be regarded as the initiation stage of joint tip deformation. Corresponding to the maximum principal strain cloud diagrams of the specimen surfaces (Fig. 11), the following patterns can be observed:

- At point a_1, the lower tip of JA and the upper tip of JD simultaneously exhibit closure and slip behavior, while the lower tip of JB and the upper tip of JC only exhibit closure behavior. Strain concentrates between the lower tip of JA and the upper tip of JD, triggering a crack propagation trend that connects the joints. After point a_1, as slip displacement initiates at the lower tip of JA and the upper tip of JD, the propagating crack begins to activate, as shown in the maximum principal strain cloud diagrams at points a_2 and a_3 in Fig. 11.
- At point a_1, the lower tip of JD simultaneously exhibits opening and slip behavior, triggering a crack propagation trend toward the specimen edge. At point a_1, the upper tip of JA simultaneously exhibits closure and slip behavior, triggering a crack propagation trend perpendicular to the adjacent joint. After point a_1, the upper tip of JA transitions to opening and reverse slip behavior, triggering a crack propagation trend toward the specimen edge.
- At point a_1, the lower tip of JC only exhibits opening behavior, triggering a crack propagation trend toward the specimen edge. After point a_1, the tip gradually transitions from opening to closure, triggering a crack propagation trend perpendicular to the adjacent joint. At point a_1, only the upper tip of JB in TR2-2 exhibits opening behavior. After point a_1, opening and slip

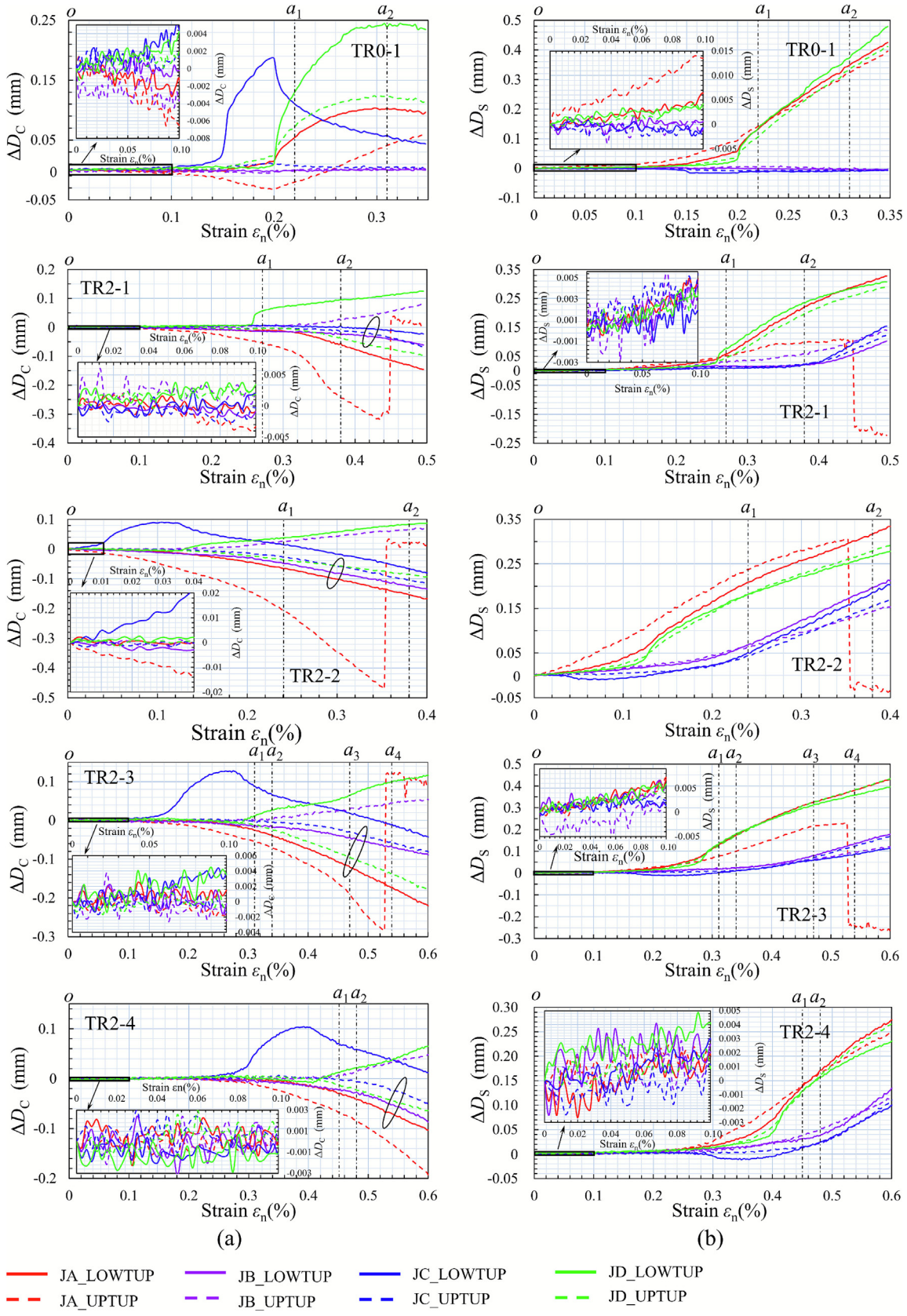

Fig. 12. Analysis of joint tip closure and slip behavior during the stress climbing stage. (a) Closure displacement curves, and (b) slip displacement curves.

behavior occur at this location in all specimens, triggering a crack propagation trend toward the specimen edge.

The above characteristics indicate that the oa_1 segment can be regarded as the activation stage of crack propagation at the joint tips, while the post-a_1 stage can be regarded as the crack propagation stage. The isolated closure behavior of the joint tips cannot trigger crack propagation. Under the influence of slip, the closure and opening behavior of the joint tips affects the direction of crack propagation (Fakoor & Shahsavar, 2021). The proportion of strain during the oa_1 relative to the oc was calculated for each specimen, yielding values of 7.4%, 10.4%, 11.0%, 14.0%, and 19.7%, respectively. Rough joints delay the initiation of tip deformation displacement, causing delayed crack propagation at the tips, which is consistent with the conclusions in Section 3.2.3.

The description of the oa in Section 3.2.3 can be further refined as follows: the oa represents the primary closure and layer-coordinated slip stage of the joints, during which cracks propagate rapidly, joints gradually connect, and specimens fracture, releasing compressive capacity and forming the stress climbing stage. Within this stage, the $oa_{1/2}$ represents the initiation of joint deformation and the activation of crack propagation. This is consistent with the conclusions of previous studies (Martin, 1997; Eberhardt et al., 1999; Amann et al., 2014).

3.3 Mechanism of uniaxial compressive strength reduction in jointed specimens due to roughness

The previous discussion qualitatively analyzed the relationships between the peak strength of the specimens, joint roughness, deformation characteristics, crack propagation, and failure modes. To determine their intrinsic connections, a correlation analysis was conducted on the aforementioned parameters. Four indicators were selected: joint roughness R, average closure level C (Eq. (13)), slip coordination S, and strain, to analyze their correlation with the peak strength S_P ($\sigma_{n,p}$). Since slip displacement and strain exhibit a significant linear correlation, only strain was included in the analysis.

$$C = \frac{\int_J -\Delta D_C \mathrm{d}s}{l_0} = \frac{\sum_J -\Delta D_C}{n}. \tag{13}$$

In the formula, ΔD_C represents the closure displacement difference between the measuring points on both sides of the joint, and l_0 is the actual length of the joint. Ideally, the closure displacement should be integrated along the contour line of the joint to be calculated, but this is not feasible in practice. Therefore, it is simplified to the arithmetic mean of a finite number of sample points, where n is the number of measurement points. In this study, the sample points shown in Fig. 8 are used for the calculation.

The S describes the discreteness of the slip displacements across different parts of the joint. Slip coordination is negatively correlated with S, the larger the value of S, the weaker the slip coordination. S is calculated using the following formula:

$$S = \sqrt{\frac{\sum_{i=1}^{n}\left(\Delta D_{S_i} - \overline{\Delta D_S}\right)^2}{n-1}}. \tag{14}$$

In the formula, ΔD_S represents the slip displacement difference between the measuring points on both sides of the joint. The correlation analysis results using Pearson correlation coefficient are shown in Fig. 13. Absolute value of the correlation coefficient is represented by the size of the circular markers: the larger the absolute value, the larger the diameter of the circle, indicating a stronger correlation. Red indicates positive correlation, while blue indicates negative correlation. To facilitate analysis, some correlation coefficients are grouped into regions. Positive correlations are highlighted with an orange background, while negative correlations are highlighted with a blue background. Each region is marked with specific symbols:

(1) P_{Ω}^{Ψ} represents a correlation analysis region formed by indicators Ψ and Ω.
(2) V_{Ω}^{Ψ} (vertical) represents a vertical correlation analysis bar formed by indicators Ψ and Ω,
(3) H_{Ω}^{Ψ} (horizontal) represents a horizontal correlation analysis bar formed by indicators Ψ and Ω.

Necessary subregions within each region are labeled with lowercase letters (e.g., a, b), and key correlation coefficients are marked with Arabic numerals (e.g., 1, 2).

(1) P_R^R shows a strong positive correlation between the roughness of JA, JD, and JA/JD. Since the rough profiles of JA and JD are derived from the same standard profile, the correlation coefficients among the three are all close to 1, validating the reliability of this correlation analysis.
(2) P_C^C shows the correlation between the average closure level of JA, JB, JC, JD, JA/JD, JB/JC, and JA/JB/JC/JD. Based on their relative independence, this region can be further divided into two subregions (a and b).
(i) ${}^{a}P_C^C$–Subregion a: Displays a weak positive correlation between the average closure levels of JA, JB, JC, and JD. This indicates that the closure behavior of individual joints is independent, with negligible interaction between them. This finding is consistent with the conclusions in Section 3.2.3 and further supports the validity of the deformation patterns described in Section 3.2.
(ii) ${}^{b}P_C^C$–Subregion b: Displays a positive correlation between the average closure levels of individual joints and joint combinations.

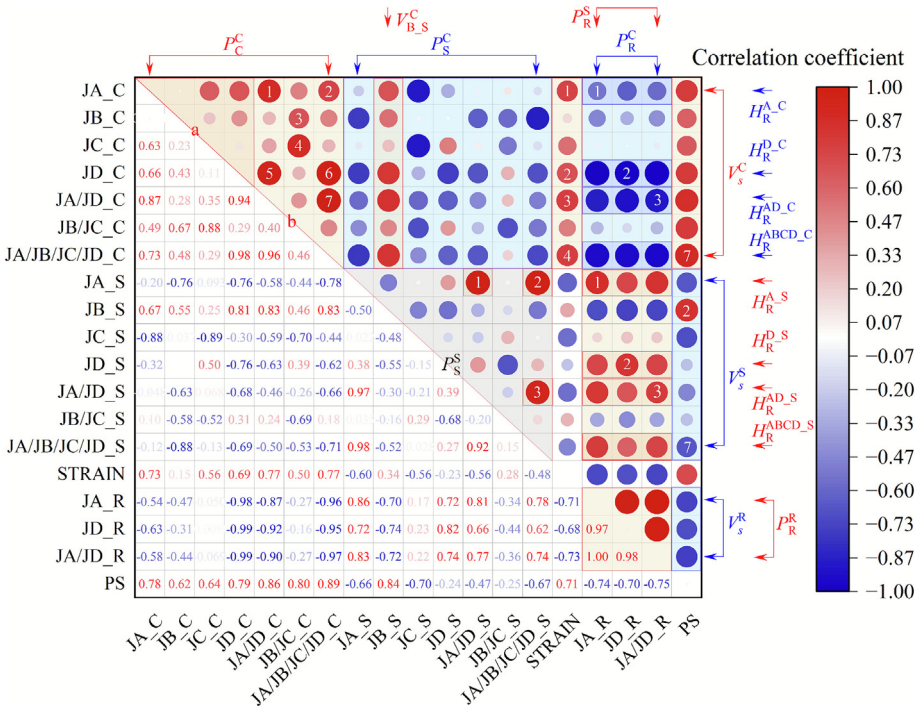

Fig. 13. Analysis of parameter correlations.

- ${}_{1,5}{}^{b}P_{C}^{C}$ indicates a strong positive correlation between the average closure levels of JA, JD, and JA/JD.
- ${}_{3,4}{}^{b}P_{C}^{C}$ indicates a strong positive correlation between the average closure levels of JB, JC, and JB/JC.
- ${}_{2,6,7}{}^{b}P_{C}^{C}$ indicates that the average closure levels of JA, JD, and JA/JD play a decisive role in the overall average closure level of the specimen's joints, with JD being the most critical. Based on the analysis in Section 3.2.3, JD consistently exhibits the smallest closure level among the four joints. This suggests that the overall average closure level of the specimen is determined by the joint with the weakest closure capacity.

(3) P_{S}^{S} shows the correlation between the slip coordination parameter S of JA, JB, JC, JD, JA/JD, JB/JC, and JA/JB/JC/JD.

- ${}_{2,6,7}P_{S}^{S}$ indicates that JA and JA/JD play a decisive role in the overall slip coordination of the specimen's joints, with JA being the most critical. Based on the analysis in Section 3.2.3, JA and JA/JD exhibit the highest overall slip coordination. This suggests that the overall slip coordination of the specimen's joints is determined by the joint layer with the best coordination.

(4) P_{S}^{C} shows a weak correlation between the average closure level of joints and the slip coordination parameter, indicating that the average closure level and slip coordination are relatively independent indicators.

(5) V_{σ}^{C} shows a strong positive correlation between the peak strength of the specimen and the average closure level of the joints.

- The correlation coefficient of ${}_{7}V_{\sigma}^{C}$ reaches 0.89, as shown in Fig. 14(a). This indicates a strong nonlinear positive relationship between the average closure level of the joints and the peak strength of the specimen. This highlights that joint closure plays a critical role in influencing the specimen's peak strength.

(6) V_{σ}^{S} shows a negative correlation between the peak strength of the specimen and the slip coordination parameter S of the joints.

- The correlation coefficient of ${}_{7}V_{\sigma}^{S}$ reaches −0.67, as shown in Fig. 14(b). This suggests a nonlinear negative relationship between the slip characteristics of the joints and the peak strength of the specimen. This highlights that joint slip is also a key factor influencing the peak strength, though its influence is relatively weaker compared to the closure level.

(7) V_{σ}^{R} shows a strong negative correlation between the peak strength of the specimen and the roughness of the joints. The correlation coefficients are all above −0.7, indicating that the roughness of the joints is another critical factor influencing the peak strength of the specimen.

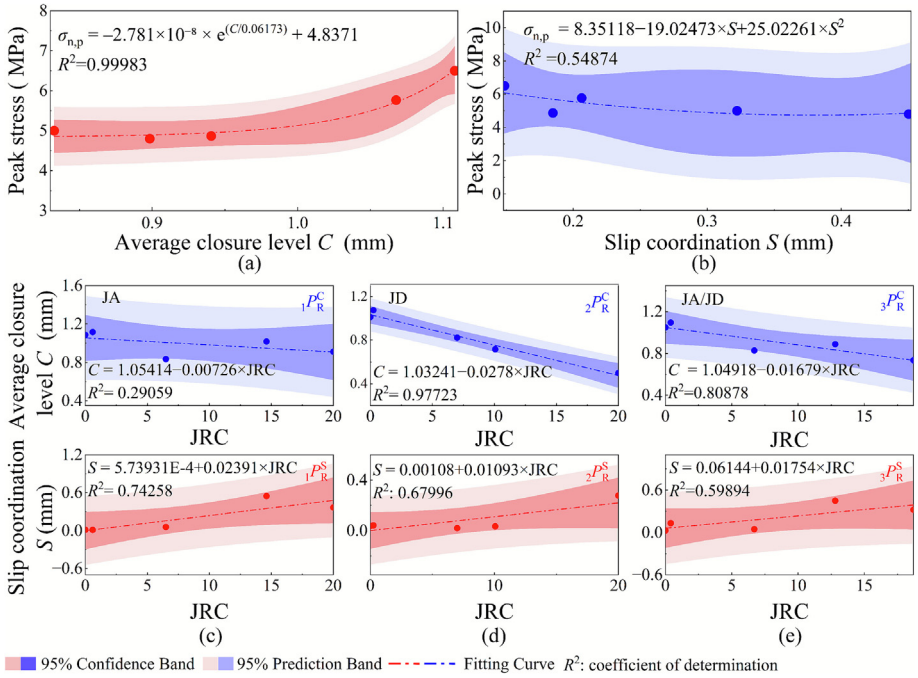

Fig. 14. Analysis of factors influencing peak strength of specimens. Relationship between the peak strength of specimens and (a) average closure level, (b) joint slip coordination, relationship between the joint roughness and joint deformation parameters of (c) joint JA, (d) JD, and (e) JA/JD.

(8) P_R^C shows a strong negative correlation between joint roughness and its closure level, which is consistent with the findings of Bandis et al. (1983). The correlation coefficients of $H_R^{D\_C}$, $H_R^{AD\_C}$, $H_R^{ABCD\_C}$ all exceed −0.9, as illustrated in Fig. 14(c)–(e), which provide detailed information about ${}_1P_R^C$, ${}_2P_R^C$, ${}_3P_R^C$.

(9) P_R^S shows a strong positive correlation between joint roughness and its slip coordination parameter, as well as a strong negative correlation between joint roughness and slip coordination. The correlation coefficients of $H_R^{A\_S}$, $H_R^{D\_S}$, $H_R^{AD\_S}$, $H_R^{ABCD\_S}$ all exceed 0.7, as illustrated in Fig. 14(c)–(e), which provides detailed information about ${}_1P_R^S$, ${}_2P_R^S$, ${}_3P_R^S$.

The above analysis quantitatively demonstrates that joint roughness influences the peak strength by affecting the average closure level and slip coordination, with the impact of the average closure level being more significant.

Combined with Fig. 5, the differences in peak strength among different specimens are primarily determined during the stress-hardening stage. Based on joint deformation behavior, the mechanism by which joint roughness affects specimen strength can be described as follows: Joint roughness influences slip coordination, which constrains the extent of joint rupture and thereby affects stress growth. Under slip conditions, roughness affects the closure level of the joints, which in turn influences the contact extent of joint walls. This ultimately determines the level of stress hardening.

4 Conclusions

(1) Under uniaxial compression, joint closure and slip behaviors exhibit significant staging and non-uniformity, jointly influenced by joint roughness, main-subordinate distribution, and layered distribution. Closure rate is primarily affected by the main-subordinate joint distribution, with main joints closing faster than subordinate joints. Slip rate is mainly influenced by the layered distribution, with joint layers closer to the main loading side slipping faster than those farther away. The sequence of closure and slip in different joint parts is significantly affected by layered distribution: joint layers closer to the main loading side close and slip progressively from top to bottom along the axial direction, while those farther from the main loading side proceed from bottom to top. Rough joints accelerate closure behavior while impeding slip capacity, causing closure to occur earlier and faster while significantly suppressing slip behavior. Main joints' closure behavior shows greater sensitivity to roughness.

(2) Isolated tip closure cannot trigger crack propagation; combined closure and opening under slip conditions determine propagation direction. For interior joint tips, closure and slip behaviors dominate crack propagation. For tips near specimen edges, alternating slip, opening, and closure behaviors control propagation. Main joints and joints closer to the loading side initiate crack propagation first.

(3) Joint deformation explains stress growth characteristics and staged failure behavior. Stage *oa* features primary joint closure with layer-coordinated slip, rapid crack propagation, and joint coalescence, forming the stress climbing stage, with sub-segment $oa_{1/2}$ representing deformation initiation and crack activation. Stage *ab* involves secondary closure and coordinated slip with localized failure, maintaining stress stability. Stage *bc* shows fully closed joints with uncoordinated slip, where wall contact creates stress hardening until overall failure.
(4) Joint roughness significantly affects uniaxial compression strength by influencing closure levels and slip coordination. Roughness constrains joint rupture by affecting slip coordination, thereby influencing stress growth. During slip, roughness redistributes joint aperture, affecting closure levels, wall contact, and stress hardening. Average closure level and slip coordination correlate negatively with roughness but positively with peak strength in a nonlinear relationship.

The above findings have important reference significance for practical geological engineering applications, particularly for underground mining pillars and cut slopes, as shown in Fig. 1. The deteriorating effect of joint roughness on specimen strength under uniaxial compression provides crucial insights for rock engineering design and stability assessment. Joint roughness characteristics should be considered when calculating pillar strength and slope stability, with design strengths appropriately reduced for rough joints to ensure adequate safety factors.

Meanwhile, the staged deformation behavior and closure-slip coordination patterns identified in this study can guide engineering monitoring strategies. The research found that joints closer to the main loading side exhibit faster closure and slip rates, indicating that critical deformation zones can be predicted based on joint distribution patterns, enabling optimization of monitoring sensor placement and development of early warning systems. Additionally, the incomplete closure behavior of rough joints indicates potential water flow pathways and weathering zones, which have important implications for the long-term stability of engineering structures.

However, this study has certain limitations that require further attention: extending the analysis to more complex triaxial and multi-axial stress conditions; investigating the effects of three-dimensional joint roughness characteristics; validating the research findings through field-scale studies and in-situ monitoring; conducting extensive experimental studies on different rock types to establish quantitative design guidelines and safety factor adjustment methods.

Data availability

The data that support the findings of this study are available from the corresponding author upon reasonable request.

CRediT authorship contribution statement

Hong Yin: Writing – review & editing, Writing – original draft, Investigation, Formal analysis, Data curation, Conceptualization. **Zehui Gao:** Writing – review & editing, Writing – original draft. **Yulong Shao:** Investigation, Formal analysis, Conceptualization. **Shuhong Wang:** Supervision, Funding acquisition. **Jae-Joon Song:** Validation, Supervision. **Ye Wang:** Writing – review & editing. **Jineon Kim:** Conceptualization. **Shan Guo:** Investigation.

Declaration of competing interest

The authors declare that they have no known competing financial interests or personal relationships that could have appeared to influence the work reported in this paper.

Acknowledgement

This work was supported by the Natural Science Foundation of China (Grant Nos. 52408417 and 52374157), the Chinese Government Joint Education Project (D20240080), and the Key Science and Technology Projects of Liaoning Province, China (2024021200-JH2/1021)

References

Afolagboye, L. O., He, J., & Wang, S. (2016). Experimental study on cracking behaviour of moulded gypsum containing two non-parallel overlapping flaws under uniaxial compression. *Acta Mechanica Sinica, 33*(2), 394–405.
Alcott, J. M., Kaiser, P. K., & Simser, B. P. (1998). Use of microseismic source parameters for rockburst hazard assessment. *Pure and Applied Geophysics, 153*(1), 41–65.
Amann, F., Ündül, O., & Kaiser, P. K. (2014). Crack initiation and crack propagation in heterogeneous sulfate-rich clay rocks. *Rock Mechanics and Rock Engineering, 47*(5), 1849–1865.
Asadizadeh, M., Hossaini, M. F., Moosavi, M., Masoumi, H., & Ranjith, P. G. (2019). Mechanical characterisation of jointed rock-like material with non-persistent rough joints subjected to uniaxial compression. *Engineering Geology, 260*, 105224.
Asadizadeh, M., Moosavi, M., Hossaini, M. F., Hedayat, A., Sherizadeh, T., & Masoumi, H. (2023). Numerical modeling of rock blocks with nonpersistent rough joints subjected to uniaxial compressive and shear loadings. *International Journal of Geomechanics, 23*(7), 04023103.
Bandis, S. C., Lumsden, A. C., & Barton, N. R. (1983). Fundamentals of rock joint deformation. *International Journal of Rock Mechanics and Mining Sciences & Geomechanics Abstracts, 20*(6), 249–268.
Barton, N., & Choubey, V. (1977). The shear strength of rock joints in theory and practice. *Rock mechanics, 10*(1), 1–54.
Bieniawski, Z. T. (1967). Mechanism of brittle fracture of rock: Part I—theory of the fracture process. *International Journal of Rock Mechanics and Mining Sciences & Geomechanics Abstracts, 4*(4), 395–406.
Brady, B. H. G., & Brown, E. T. (2006). *Rock mechanics: For underground mining*. Springer.
Cao, R., Yao, R., Meng, J., Lin, Q., & Li, S. (2020). Failure mechanism of non-persistent jointed rock-like specimens under uniaxial loading: Laboratory testing. *International Journal of Rock Mechanics and Mining Sciences, 132*, 104341.
Chen, L., Wang, C. P., Liu, J. F., Liu, J., Wang, J., Jia, Y., & Shao, J. F. (2015). Damage and plastic deformation modeling of beishan granite under compressive stress conditions. *Rock Mechanics and Rock Engineering, 48*(4), 1623–1633.
Chen, X., Liao, Z.-H., & Peng, X. (2013). Cracking process of rock mass models under uniaxial compression. *Journal of Central South University, 20*(6), 1661–1678.

Chen, X., Liao, Z., & Peng, X. (2012). Deformability characteristics of jointed rock masses under uniaxial compression. *International Journal of Mining Science and Technology, 22*(2), 213–221.
Chen, Y., & Guo, B. (2020). Crack closure effect and energy dissipation model for rocks under uniaxial compression. *Geotechnical and Geological Engineering, 38*(1), 621–629.
Cook, N. G. W. (1992). Natural joints in rock: Mechanical, hydraulic, and seismic behavior and properties under normal stress. *International Journal of Rock Mechanics and Mining Sciences & Geomechanics Abstracts, 29*(3), 198–223.
Cui, P., Ge, Y., Li, S., Li, Z., Xu, X., Zhou, G. G. D., Chen, H., Wang, H., Lei, Y., Zhou, L., Yi, S., Wu, C., Guo, J., Wang, Q., Lan, H., Ding, M., Ren, J., Zeng, L., Jiang, Y., & Wang, Y. (2022). Scientific challenges in disaster risk reduction for the Sichuan–Tibet Railway. *Engineering Geology, 309*, 106837.
Eberhardt, E., Stimpson, B., & Stead, D. (1999). Effects of grain size on the initiation and propagation thresholds of stress-induced brittle fractures. *Rock Mechanics and Rock Engineering, 32*(2), 81–99.
Erdogan, F., & Sih, G. C. (1963). On the crack extension in plates under plane loading and transverse shear. *Journal of Fluids Engineering, Transactions of the ASME, 85*(4), 519–525.
Esterhuizen, G. S., Dolinar, D. R., & Ellenberger, J. L. (2011). Pillar strength in underground stone mines in the United States. *International Journal of Rock Mechanics and Mining Sciences, 48*(1), 42–50.
Fakoor, M., & Shahsavar, S. (2021). The effect of T-stress on mixed mode I/II fracture of composite materials: Reinforcement isotropic solid model in combination with maximum shear stress theory. *International Journal of Solids and Structures, 229*, 111145.
Fereshtenejad, S., & Song, J. J. (2021). Applicability of powder-based 3D printing technology in shear behavior analysis of rock mass containing non-persistent joints. *Journal of Structural Geology, 143*, 104251.
Gao, Y. T., Wu, T. H., & Zhou, Y. (2021). Application and prospective of 3D printing in rock mechanics: A review. *International Journal of Minerals, Metallurgy and Materials, 28*(1), 1–17.
Goodman, R. E. (1974). The mechanical properties of joints. In *Proceedings of the third international congress international society of rock mechanic* (pp. 127–140). Denver: ISRM.
Griffith, A. A. (1921). The phenomena of rupture and flow in solids. *Philosophical Transactions of the Royal Society A, 221*, 163–198.
Haeri, H., Sarfarazi, V., & Marji, M. F. (2021). Experimental and numerical investigation of uniaxial compression failure in rock-like specimens with l-shaped nonpersistent cracks. *Iranian Journal of Science and Technology, Transactions of Civil Engineering, 45*(4), 2555–2575.
Hoek, E., & Bieniawski, Z. T. (1965). Brittle fracture propagation in rock under compression. *International Journal of Fracture Mechanics, 1*(3), 137–155.
Hopkins, D. L. (2000). The implications of joint deformation in analyzing the properties and behavior of fractured rock masses, underground excavations, and faults. *International Journal of Rock Mechanics and Mining Sciences, 37*(1/2), 175–202.
Hu, G., Li, Y., & Ma, G. (2021). Research on the size effect of roughness on rock uniaxial compressive strength and characteristic strength. *Science and Engineering of Composite Materials, 28*(1), 613–627.
Huang, C., Yang, W., Duan, K., Fang, L., Wang, L., & Bo, C. (2019). Mechanical behaviors of the brittle rock-like specimens with multi-non-persistent joints under uniaxial compression. *Construction and Building Materials, 220*, 426–443.
Huang, D., Tang, W., & Li, X. Q. (2023). Numerical modeling and damage evolution research on the effect of joint geometrical parameters in nonpersistent jointed rock masses. *Bulletin of Engineering Geology and the Environment, 82*(4), 137.
Jiao, Y., Zuo, Y., Wen, Z., Chen, Q., Zheng, L., Lin, J., ... Du, S. et al. (2024). Crack-tip propagation laws and energy evolution of fractured sandstone. *Engineering Failure Analysis, 166*, 108832.
Johansson, F., & Stille, H. (2014). A conceptual model for the peak shear strength of fresh and unweathered rock joints. *International Journal of Rock Mechanics and Mining Sciences, 69*, 31–38.
Kumar, S., Tiwari, G., Parameswaran, V., & Das, A. (2022). Rate-dependent mechanical behavior of jointed rock with an impersistent joint under different infill conditions. *Journal of Rock Mechanics and Geotechnical Engineering, 14*(5), 1380–1393.
Li, H., Lai, Y., Zhang, M., Chen, Y., Ma, Q., Liang, T., & Gao, X. (2024). Elastoplastic damage behavior of quasi-brittle rocks considering crack closure evolution. *Computers and Geotechnics, 166*, 106031.
Li, Y., & Zhang, Y. (2015). Quantitative estimation of joint roughness coefficient using statistical parameters. *International Journal of Rock Mechanics and Mining Sciences, 77*, 27–35.
Liu, Z., Zhang, C., Zhang, C., Gao, Y., Zhou, H., & Chang, Z. (2019). Deformation and failure characteristics and fracture evolution of cryptocrystalline basalt. *Journal of Rock Mechanics and Geotechnical Engineering, 11*(5), 990–1003.
Lu, Y. L., Elsworth, D., & Wang, L. G. (2013). Microcrack-based coupled damage and flow modeling of fracturing evolution in permeable brittle rocks. *Computers and Geotechnics, 49*, 226–244.
Luo, P. F., Chao, Y. J., Sutton, M. A., & Peters, W. H. III, (1993). Accurate measurement of three-dimensional deformations in deformable and rigid bodies using computer vision. *Experimental Mechanics, 33*(2), 123–132.
Ma, G., Hu, T., & Li, Z. (2024). Binder jetting 3D printing rock analogs using magnesium phosphate cement. *Construction and Building Materials, 420*, 135620.
Martin, C. D. (1997). Seventeenth Canadian geotechnical colloquium: The effect of cohesion loss and stress path on brittle rock strength. *Canadian Geotechnical Journal, 34*(5), 698–725.
Park, C. H., & Bobet, A. (2009). Crack coalescence in specimens with open and closed flaws: A comparison. *International Journal of Rock Mechanics and Mining Sciences, 46*(5), 819–829.
Pradhan, S. P., & Siddique, T. (2020). Stability assessment of landslide-prone road cut rock slopes in Himalayan terrain: A finite element method based approach. *Journal of Rock Mechanics and Geotechnical Engineering, 12*(1), 59–73.
Ren, L., Zhao, L. Y., & Niu, F. J. (2022). A physically-based elastoplastic damage model for quasi-brittle geomaterials under freeze-thaw cycles and loading. *Applied Mathematical Modelling, 106*, 276–298.
Ren, L., Zhao, L. Y., Niu, F. J., Lai, Y. M., & Shao, J. F. (2023). A nonlinear constitutive model for whole stress–strain behaviors of compressed rocks incorporating crack closure effect. *International Journal for Numerical and Analytical Methods in Geomechanics, 47*(11), 2003–2026.
Shan, R., Liu, N., Sun, P., Zhao, Z., Dong, R., Dou, H., Meng, H., & Bai, Y. (2025). Experimental and numerical simulation study of rough jointed rock samples under triaxial compression conditions. *Engineering Fracture Mechanics, 314*, 110707.
Shao, Y., Kim, J., He, C., Yin, H., Mehrishal, S., Yao, C., & Song, J. J. (2024a). Experimental investigation of the coupled effects of bedding planes and flaws on fracture evolution of soft bedded rocks based on 3D printing and DIC technologies. *Theoretical and Applied Fracture Mechanics, 133*(Part A).
Shao, Y., Kim, J., Yang, J., Song, J. J., & Moon, J. (2024b). Experimental study on strength enhancement and porosity variation of 3D-printed gypsum rocks: insights on vacuum infiltration post-processing. *Rock Mechanics and Rock Engineering, 57*(9), 6763–6786.
Shao, Y., Yang, J., Kim, J., He, C., Song, J. J., Yin, H., & Leem, J. (2025). Strain localization-controlled rock failure using digital volume correlation technology: In situ compression tests on 3D-printed rock-like samples with a single initial flaw. *Journal of Rock Mechanics and Geotechnical Engineering, 17*(7), 4329–4348.
Shao, Y., Yang, J., Kim, J., Mehrishal, S., & Song, J. J. (2024c). Quantitative analysis and 3D visualization of crack behavior in 3D-printed rock-like specimens with single flaw using in-situ micro-CT imaging. *Rock Mechanics and Rock Engineering, 57*(9), 7271–7291.
Sih, G. C. (1974). Strain-energy-density factor applied to mixed mode crack problems. *International Journal of Fracture, 10*, 305–321.
Tang, Y., Okubo, S., Xu, J., & Peng, S. (2019). Progressive failure behaviors and crack evolution of rocks under triaxial compression by 3D digital image correlation. *Engineering Geology, 249*, 172–185.
Tse, R., & Cruden, D. M. (1979). Estimating joint roughness coefficients. *International Journal of Rock Mechanics and Mining Sciences & Geomechanics Abstracts, 16*(5), 303–307.
Walton, G., Hedayat, A., Kim, E., & Labrie, D. (2017). Post-yield strength and dilatancy evolution across the brittle–ductile transition in Indiana limestone. *Rock Mechanics and Rock Engineering, 50*(7), 1691–1710.
Wang, B., Gerolymatou, E., & Jin, A. (2023a). Study on mechanical and fracture characteristics of rock-like specimens with rough non-persistent joints by YADE DEM simulation. *Computers and Geotechnics, 158*, 105382.
Wang, D., He, S., & Tannant, D. D. (2019). A strain based method for determining the crack closure and initiation stress in compression tests. *KSCE Journal of Civil Engineering, 23*(4), 1819–1828.

Wang, M., Lu, Z., Zhao, Y., & Wan, W. (2025). Numerical study on the strength and fracture of rock materials with multiple rough preexisting fissures under uniaxial compression using particle flow code. *Computational Particle Mechanics, 12*(1), 453–477.

Wang, Y., Lu, H., & Wu, J. (2021). Experimental investigation on strength and failure characteristics of cemented paste backfill-rock composite under uniaxial compression. *Construction and Building Materials, 304*, 124629.

Wang, Y., Yang, X., Li, W., & Qiao, W. (2023b). Experimental study on the effect of anchored bolts on failure and strength behavior of nonpersistent jointed rock model. *Bulletin of Engineering Geology and the Environment, 82*(3), 95.

Wu, X., Jiang, L., Tao, M., Mitri, H. S., & Xiang, G. (2024). Dynamic behaviors and bolt-strengthening effect of sand-powder 3D printing rock analog under static and dynamic coupled loading. *Construction and Building Materials, 411*, 134723.

Xie, S., Han, Z., & Lin, H. (2022). A quantitative model considering crack closure effect of rock materials. *International Journal of Solids and Structures, 251*, 111758.

Yang, S. Q., Chen, M., Huang, Y. H., Jing, H. W., & Ranjith, P. G. (2020). An experimental study on fracture evolution mechanism of a non-persistent jointed rock mass with various anchorage effects by DSCM, AE and X-ray CT observations. *International Journal of Rock Mechanics and Mining Sciences, 134*, 104469.

Ye, Y., Ma, J., Wu, Z., & Zeng, Y. (2021). A novel 3D-FDEM method using finite-thickness cohesive elements to simulate the nonlinear mechanical behaviors of rocks. *Computers and Geotechnics, 140*, 10447.

Yin, H., Wang, S., Song, J. J., Gao, Z., Kim, J., & Shao, Y. (2024). Mechanical behavior of rock-like specimens with 3D nonpenetrating and nonpersistent rough joints under uniaxial compression: Experimental study. *Bulletin of Engineering Geology and the Environment, 83*(6), 239.

Yuan, P., Li, A., Chen, C., & Lu, X. (2023). Experimental study of uniaxial compressive mechanical properties of rough jointed rock masses based on 3D printing. *Applied Rheology, 33*(1), 20230114.

Zhang, S., Chen, W., & Liu, H. (2023). Dynamic response of tunnels surrounded by thawing permafrost with anisotropic frost heave in cold regions: considering the movement of the frozen interface. *Journal of Engineering Mechanics, 149*(2), 04022112.

Zhang, Z., Wang, S., Yang, T., Dong, F., Gao, Z., & Wang, D. (2024). Influence of contact characteristics on nonlinear flow and eddy development in three-dimensional fractures under normal stress. *Bulletin of Engineering Geology and the Environment, 83*(4), 129.

Zhou, X. P., Cheng, H., & Feng, Y. F. (2013). An experimental study of crack coalescence behaviour in rock-like materials containing multiple flaws under uniaxial compression. *Rock Mechanics and Rock Engineering, 47*(6), 1961–1986.